

Effects of turbulence on the geometric collision rate of sedimenting droplets. Part 1. Results from direct numerical simulation

This article has been downloaded from IOPscience. Please scroll down to see the full text article.

2008 New J. Phys. 10 075015

(<http://iopscience.iop.org/1367-2630/10/7/075015>)

View [the table of contents for this issue](#), or go to the [journal homepage](#) for more

Download details:

IP Address: 128.117.174.131

The article was downloaded on 14/10/2011 at 17:42

Please note that [terms and conditions apply](#).

Effects of turbulence on the geometric collision rate of sedimenting droplets.

Part 1. Results from direct numerical simulation

Orlando Ayala¹, Bogdan Rosa¹, Lian-Ping Wang^{1,3}
and Wojciech W Grabowski²

¹ Department of Mechanical Engineering, 126 Spencer Laboratory, University of Delaware, Newark, Delaware 19716-3140, USA

² Mesoscale and Microscale Meteorology Division, National Center for Atmospheric Research, PO Box 3000, Boulder, Colorado 80307-3000, USA
E-mail: lwang@udel.edu

New Journal of Physics **10** (2008) 075015 (31pp)

Received 17 December 2007

Published 31 July 2008

Online at <http://www.njp.org/>

doi:10.1088/1367-2630/10/7/075015

Abstract. There have been relatively few studies of turbulent collision rate of sedimenting droplets in the context of cloud physics, for which both the gravitational settling and inertial effects must be simultaneously considered. In this study, direct numerical simulations (DNS) were used to study the geometric collision rates of cloud droplets. Both Stokes drag law and a nonlinear drag law were considered, but the droplet–droplet local aerodynamic interactions were not included. Typical droplet and turbulence parameters of convective clouds were used to determine the flow dissipation rate ϵ , characteristic Stokes numbers, and the nondimensional terminal velocities. DNS results from a large number of runs covering the ϵ range from 10 to 400 cm² s⁻³ and droplet sizes from 10 to 60 μ m in radius are presented. These results show that air turbulence can increase the geometric collision kernel by up to 47%, relative to geometric collision by differential sedimentation. This is due to both a moderate enhancement of the radial relative velocity between droplets and a moderate level of pair nonuniform concentration due to local droplet clustering. The turbulence enhancements increase with the flow dissipation rate and flow Reynolds number. Comparisons with related DNS studies show that our results confirm and extend the previous findings. The mean settling velocity of droplets in a turbulent flow was also obtained, showing that a maximum increase relative to the terminal velocity

³ Author to whom any correspondence should be addressed.

occurs for $20\ \mu\text{m}$ cloud droplets. This agrees with a previous theory based on simple vortex flows and confirms the importance of a new nondimensional parameter $\tau_p^3 g^2 / \nu$ for sedimenting droplets, where τ_p is the droplet inertial response time, g is the gravitational acceleration and ν is the air kinematic viscosity. Limitations of DNS and future directions are also noted.

Contents

1. Introduction	2
2. Description of cloud turbulence and cloud droplets	5
2.1. Characteristics of air turbulence	5
2.2. Characteristics of cloud droplets	6
3. Kinematic formulation of geometric collision kernel	8
4. DNS	9
4.1. Turbulent flow field	9
4.2. Motion of droplets	10
4.3. Collision detections and computation of kinematic properties	11
5. Results	12
5.1. Validation of the kinematic kernel against the dynamic kernel	12
5.2. Geometric collision kernel and related kinematic properties	14
5.3. Average settling velocity	25
5.4. The nonlinear drag effect	26
6. Summary and concluding remarks	29
Acknowledgments	30
References	30

1. Introduction

In recent years, there has been a renewed interest in studying the effects of air turbulence on the collision–coalescence growth of cloud droplets [1]–[6]. This is motivated by the need to resolve an open issue in cloud physics [7, 8] concerning the growth of cloud droplets in the size range from 10 to $50\ \mu\text{m}$ in radius (i.e. the so-called size gap), for which neither the condensation nor the gravitational collision–coalescence mechanism is effective [5]. Observations of radar reflectivity in tropical regions suggest that rain could form in cumulus clouds by warm rain process in approximately 15 to 20 min [9, 10]. Theoretical predictions based on the gravitational–coalescence mechanism alone, however, would require a time interval in the order of an hour for droplets to grow from 20 to $100\ \mu\text{m}$ in radius (the actual time depends on the cloud water content, initial droplet size spectrum, updraft speed, etc, see Pruppacher and Klett [7]). Therefore, there appears to be a factor of 2 or more difference between the predicted observed growth time. The onset of drizzle-size ($\sim 100\ \mu\text{m}$ in radius) raindrops is still poorly understood in many precipitating cloud systems.

It has long been speculated that the effect of air turbulence could play an important role in closing the size gap [12]–[14], although several other alternative explanations have also been proposed, including growth by ultragiant particles, entrainment-induced spectral broadening

and effects of pre-existing clouds [11, 15, 16]. Resolving this open issue quantitatively is crucial in view of the fact that warm rain accounts for 31% of the total rain fall and 72% of the total rain area in the tropics [17].

Here, we shall focus on the effects of air turbulence on droplet growth by collision–coalescence. At least four effects of turbulence have been documented to date. The first is the effect of local shear and air acceleration on the relative *fluctuating* motion of the droplets. The increased relative motion is caused by the viscous drag acting on the droplets as well as the differential inertial response of the droplets to local fluid acceleration. This effect was first described qualitatively by Arenberg [12] and semi-analytically by Gabilly [18] and East and Marshall [19]. Saffman and Turner [20] developed a rigorous theoretical formulation to account for the enhanced relative motion by turbulence on collision rates applicable to weak-inertia droplets. Further extensions of Saffman and Turner’s theory are found in [21]–[24]. In the context of cloud droplets, this enhanced relative motion by turbulence has been proposed as a mechanism to generate a significant increase in collision rates among cloud droplets when compared with the gravitational collision–coalescence [25]–[28].

The second effect results from the enhanced average droplet-pair density due to local preferential concentration. Maxey [29] showed theoretically that inertial particles tend to accumulate in local regions of low vorticity and high strain rate due to an inertial bias similar to the centrifugal effect. This preferential concentration was later confirmed in direct numerical simulations (DNS) [30, 31]. Since local collision rates are proportional to the second moment of local droplet concentrations, the preferential concentration may significantly increase the average collision rate. This effect on collision rate was described theoretically through an enhancement factor referred to as the radial distribution function (RDF) [32]–[34]. Falkovich *et al* [2] argued theoretically that the preferential concentration can increase the average collision kernel by a factor of 10 in high Reynolds-number turbulence due to strong intermittency of the local turbulence microstructures.

The third effect is the increased settling velocity by air turbulence. Sedimenting particles bias their trajectories toward regions of downward fluid motion around vortices and could settle significantly faster than the terminal velocity [29, 31, 35]. Since the increased settling occurs selectively for droplets with a certain range of terminal velocity and inertial response time [31, 35], it has been argued that this effect could alter the collision–coalescence growth by modified relative *mean* motion of droplets in clouds [4, 36].

The fourth effect concerns the collision efficiency between droplets due to local aerodynamic interactions. While the collision efficiencies between droplets without air turbulence have been relatively well studied [13, 37, 38], there have been very few studies on collision efficiency in turbulent clouds [34], [39]–[43]. Qualitatively, we expect modifications of collision efficiency by air turbulence, since the background air flow alters the magnitude and orientation of droplet–droplet relative motion and since collision efficiency depends sensitively on the size-dependent relative motion for the size range of interest [37]. Some limited quantitative assessment of the collision efficiency enhancement by turbulence has been presented in [34].

We mention in passing that there are a few studies on the effects of turbulence on the diffusional growth [44]–[47]. Shaw *et al* [44] speculated that preferential concentration might result in significant supersaturation fluctuations that could broaden the size spectrum by diffusional growth. Three-dimensional DNS by Vaillancourt *et al* [46, 47] for sedimenting droplets under conditions of typical cumulus clouds showed that, while turbulence does cause

supersaturation fluctuations, it decreases the correlation time of small-scale supersaturation fluctuations seen by the droplets. The net effect of small-scale turbulence on the size spectrum by diffusional growth is found to be insignificant. On the other hand, a two-dimensional DNS study by Celani *et al* [48] suggests that large-scale supersaturation fluctuations could lead to a correlation between droplet trajectories and supersaturation, and thus stochastic broadening of droplet size distribution.

The brief review above shows both the multifacetedness and complexity of the effects of air turbulence on droplet growth by collision–coalescence. A complete description of all the aspects requires a full knowledge of air turbulent motion and dynamics of droplet–fluid interactions and droplet–droplet interactions, all of which are three-dimensional and time-dependent in nature. This represents a complex turbulent multiphase flow problem.

The main objective of this paper is to quantify the first three effects of turbulence discussed above, using DNS in which the small-scale dynamics of air turbulence is computed precisely. Previously, DNS have been used to study collision rates of non-sedimenting particles [32, 33, 49]. In the context of cloud droplets, gravitational sedimentation must be included [14, 45, 47]. We shall limit our study to the parameter region (i.e. relative inertia and terminal velocity) relevant to atmospheric clouds [12].

There have been very few DNS studies reporting geometric collision rates of sedimenting cloud droplets [34, 50, 51]. We will quantify the individual effects of turbulence and examine how they vary with the droplet sizes and flow dissipation rate, and, to a limited extent, with the flow Reynolds number. This paper extends the work of [34] where collision statistics for one specific size combination (20 and 25 μm) were reported. The DNS approach used in this paper is very similar to the work of Franklin *et al* [50, 51]. We note that the large-scale forcing scheme used in this work (Langevin stochastic method of Eswaran and Pope [52]) differs from the deterministic forcing method [53] adopted by Franklin *et al*. It is not clear which scheme is more appropriate for small-scale cloud turbulence. The deterministic scheme may bring more coherence to turbulent eddies, this may explain why the collision kernels in [50, 51] are somewhat larger than our results (see figure 5). Given a very few DNS studies of geometric collision rate for cloud droplets and the incomplete exploration of the parameter space so far, the large amount of DNS data to be presented here, together with the results in [50, 51], provide a more complete quantitative description of the turbulent collision kernel of cloud droplets.

The paper is organized as follows. In section 2, a general description of cloud turbulence and cloud droplets is given to help specify the relevant parameters of the problem. The kinematic formulation of geometric collision kernel is reviewed in section 3, which will be used to validate our code development and guide the interpretation of DNS results. The main elements of DNS are described in section 4. DNS results are compiled and discussed in section 5: these include results and comparison of kinematic collision kernel and dynamic collision kernel, results on radial relative velocity and RDF and on average settling velocity. Results based on a nonlinear drag are compared with these based on the Stokes drag. We have also compared our DNS results with the recent DNS results of Franklin *et al* [50, 51]. Finally, conclusions are summarized in section 6. In another contribution to this focus issue [54], we will develop a theoretical parameterization of the turbulent collision kernel and compare the theory to the DNS results in this paper.

Table 1. Typical cloud turbulence dissipation rate and Kolmogorov scales.

ϵ ($\text{cm}^2 \text{s}^{-3}$)	τ_k (s)	η (cm)	v_k (cm s^{-1})
10	0.1304	0.1488	1.142
100	0.0412	0.0837	2.031
400	0.0206	0.0592	2.872

2. Description of cloud turbulence and cloud droplets

2.1. Characteristics of air turbulence

We consider here the collision rates of small water droplets inside typical cumulus clouds where the air turbulence is expected to be nearly isotropic and homogeneous. Vaillancourt and Yau [14] stated two reasons for this expectation. Firstly, the environmental vertical stratification can be neglected on scales smaller than about 100 m (typical integral length scale of turbulence). Secondly, at distances sufficiently far from mixing regions of clouds, the small-scale flow is primarily driven by nonlinear energy transfer from larger scales.

Since the local volume fraction of droplets in atmospheric clouds is typically in the order of 10^{-6} (or mass loading in the order of 10^{-3}), it is assumed that the background air flow $\mathbf{U}(\mathbf{x}, t)$ is not affected by the presence of droplets. The dissipation-range fluid motion in the air turbulence is assumed to govern the collision rate of droplets, and it is characterized by the Kolmogorov length, velocity and timescales

$$\eta = (\nu^3/\epsilon)^{1/4}, \quad v_k = (\nu\epsilon)^{1/4}, \quad \tau_k = (\nu/\epsilon)^{1/2}, \quad (1)$$

where ϵ is the average air-flow kinetic dissipation rate and ν is the air kinematic viscosity. Observations suggest that ϵ could vary from 1 to $1000 \text{ cm}^2 \text{ s}^{-3}$ in cumulus and stratocumulus clouds [13, 14] yielding a range of η from $470 \mu\text{m}$ to 2.6 mm . In this work, three intermediate values of the dissipation rate were considered and they are listed in table 1 along with the Kolmogorov scales when the air viscosity ν is taken to be $0.17 \text{ cm}^2 \text{ s}^{-1}$. Another important parameter that characterizes the turbulence in cloud is the Taylor-microscale Reynolds number R_λ defined as $R_\lambda \equiv u'\lambda/\nu$, where λ is the transverse Taylor microscale ($\lambda \equiv u'/\langle(\partial u_1/\partial x_1)^2\rangle^{1/2} = (15\nu u'^2/\epsilon)^{1/2}$) and u' is the rms fluctuation velocity. This Reynolds number determines the range of scales in a turbulent flow. R_λ achievable in DNS is typically in the order of 10^2 and is roughly two orders of magnitude smaller than the R_λ value in real clouds. Since the dynamics of cloud droplets is governed mainly by the dissipation-range fluid motion, it is assumed that the value of ϵ is of primary importance and that R_λ is of secondary importance. However, this does not exclude the possibility that flow Reynolds number can play a role: (a) droplets respond to a range of turbulent eddies, including large-scale motion in low-Reynolds number DNS, (b) the limited scales in DNS do not really allow separation of effects of large and small scales and (c) there exists a possibility that small-scale eddy structure is connected to large-scale eddies through non-local eddy interactions.

Table 2. Basic properties of cloud droplets.

a (μm)	τ_p (s)	v_p (cm s^{-1})	Re_{p0}	$f(Re_{p0})$
10	0.0013	1.272	0.015	1.008
20	0.0052	4.959	0.116	1.034
30	0.0118	10.717	0.378	1.077
40	0.0209	18.089	0.851	1.134
50	0.0327	26.624	1.566	1.204
60	0.0471	35.944	2.537	1.284

2.2. Characteristics of cloud droplets

We shall focus our study on droplets of radii from 10 to 60 μm as these are most relevant to the size gap problem in warm rain microphysics. These droplets are one to two orders of magnitude smaller than the smallest eddies in the air turbulence. They move in response to the local fluid motion (i.e. velocity and acceleration) and the gravitational body force. Neglecting the droplet–droplet aerodynamic interaction, each droplet is assumed to move independently of other droplets in the system. The motion of each droplets is described by its instantaneous location $\mathbf{Y}(t)$ and velocity $\mathbf{V}(t)$. Under the above conditions and noting that the density of water droplets (ρ_w) is much larger than the air density ρ , the equation of motion of any given droplet of radius a is

$$\frac{d\mathbf{V}(t)}{dt} = f(Re_p) \frac{\mathbf{U}(\mathbf{Y}(t), t) - \mathbf{V}(t)}{\tau_p} + \mathbf{g}, \quad (2)$$

where $\mathbf{U}(\mathbf{Y}(t), t)$ is the fluid flow velocity as seen by a stationary observer at the droplet location and \mathbf{g} is the gravitational acceleration. The Stokes inertial response time, $\tau_p \equiv 2\rho_w a^2 / 9\rho\nu$, is the characteristic time for the particle to react to changes in the flow. The nonlinear factor $f(Re_p)$ models the departure from the Stokes drag law and may be given as [53]

$$f(Re_p) = 1 + 0.15 Re_p^{0.687}, \quad (3)$$

where, in general, the droplet Reynolds number is defined in terms of the relative velocity between the droplet and the background fluid as $Re_p = 2a|\mathbf{V} - \mathbf{U}|/\nu$, provided the background fluid velocity varies on scales much larger than the size of the droplet. For the case of steady motion in still air ($\mathbf{U} = 0$), the terminal velocity of a droplet is given as

$$v_p = \frac{\tau_p |\mathbf{g}|}{f(Re_{p0})}, \quad (4)$$

where the droplet Reynolds number in stagnant air is defined as $Re_{p0} \equiv 2av_p/\nu$. Unlike Re_{p0} , the droplet Reynolds number Re_p for a given droplet size is a random variable with a range of values due to velocity fluctuations in a turbulent flow. The still air Re_{p0} only provides a rough estimate of the mean value of Re_p .

In table 2, pertinent parameters of the droplets are listed assuming $\rho = 0.001 \text{ g cm}^{-3}$ and $\rho_w = 1.0 \text{ g cm}^{-3}$. The particle Reynolds number is important because particles with large Re_p may cause extended disturbance flows with wake or vortex shedding. As the particle Reynolds numbers are small, no vortex shedding is expected and the disturbance flows by particles are

Table 3. Characteristic scales of cloud droplets.

a (μm)	ϵ ($\text{cm}^2 \text{s}^{-3}$)								
	10			100			400		
	St	Sv	a/η	St	Sv	a/η	St	Sv	a/η
10	0.010	1.113	0.007	0.032	0.626	0.011	0.063	0.442	0.017
20	0.040	4.343	0.013	0.127	2.442	0.024	0.253	1.727	0.034
30	0.090	9.385	0.020	0.285	5.278	0.036	0.570	3.732	0.051
40	0.160	15.841	0.027	0.507	8.908	0.047	1.014	6.299	0.067
50	0.250	23.316	0.033	0.792	13.111	0.059	1.585	9.271	0.084
60	0.361	31.478	0.040	1.141	17.701	0.071	2.282	12.516	0.101

locally contained. We can conclude from table 2 that the nonlinear drag correction may be neglected for droplets of radii less than $30 \mu\text{m}$, if the droplet motion due to turbulence is weak compared with the gravity effect. We shall first adopt the linear Stokes drag in our simulations, but will discuss the use of nonlinear drag later in section 5.4. Another reason for using Stokes drag is that a more consistent treatment of droplet–droplet aerodynamic interactions is possible using a hybrid direct simulation approach, as shown in [34, 56].

In table 3, the cloud droplet characteristics are compared to the characteristic scales of dissipation-range air motion. The two nondimensional numbers describing the relative inertia and settling rate are

$$St = \frac{\tau_p}{\tau_k}, \quad Sv = \frac{v_p}{v_k}. \quad (5)$$

The Stokes number St is a key parameter governing the droplet response to the fluid motion and the resulting effects of turbulence on the collision rate. If the particle reacts instantaneously to any acceleration of the flow (small Stokes number), then it behaves as a tracer. If the particle responds very slowly to the accelerations in the flow (large Stokes number), then the effect of fluid acceleration may not be felt by the particle. A strong interaction between the flow and the particles in a vertical flow occurs when the Stokes number is in the order of one [31]. It is stressed that ranges of time and length scales coexist in a turbulent flow. We chose to define the nondimensional parameters with Kolmogorov scales in this work since the relative motion of the droplets is of primary concern. Sv also plays a very important role in determining the interaction time with turbulent eddies as the droplet settles under gravity and in determining whether the droplet mean settling velocity differs from its terminal velocity [35]. Sv can also be viewed as the ratio of the small-eddy turnover time (assumed to be τ_k) and the time it takes for the particle to sediment across the eddy. If the ratio is much larger than one, then the particle will rapidly sediment through the eddy, thereby leading to weak particle–eddy interaction. On the other hand, if the ratio is much smaller than one, sedimentation does not play any significant role in reducing the time of particle–eddy interaction.

We display in figure 1 the dependence of Sv and St on ϵ and a for a larger range of ϵ that is relevant to clouds. From both table 3 and figure 1, we conclude that the Stokes number is typically less than one whereas the nondimensional settling is typically larger than one. Consistent with the conclusion of Vaillancourt and Yau [14], the gravitational effect is always important for cloud droplets. More importantly, both nondimensional parameters can vary by

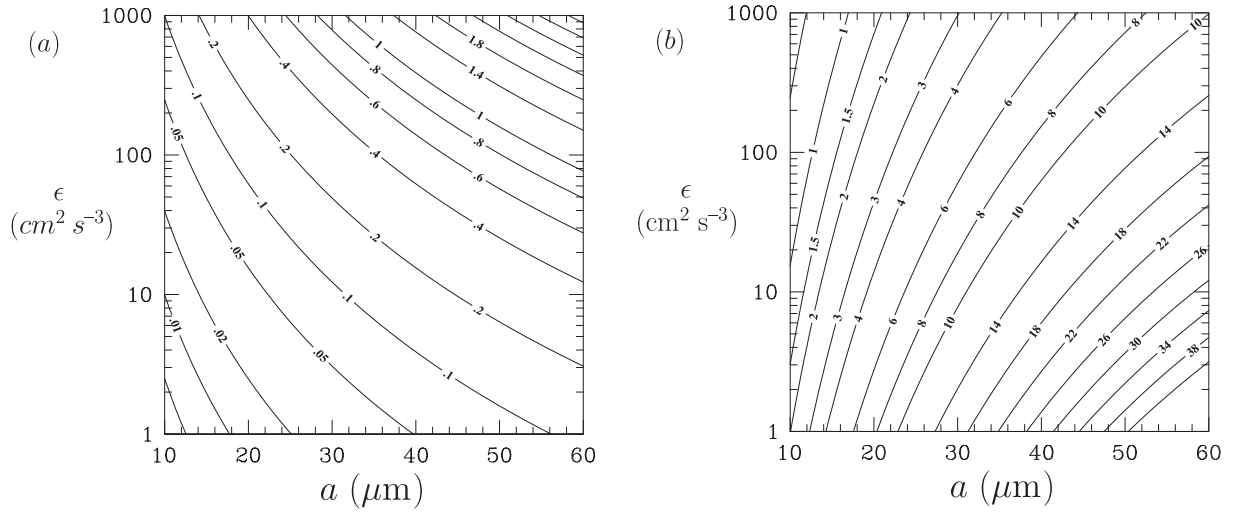


Figure 1. Contour plots of (a) Stokes number St and (b) nondimensional settling velocity Sv as a function of flow dissipation rate ϵ and droplet radius a .

more than one order of magnitude even for such a narrow size range from 10 to 60 μm . The range of values for St in the table shows that the relative importance of turbulent inertia effect in the cloud context varies. Most turbulent effects on particle collision rate tend to increase with St for $St < 1$ according to previous studies for non-sedimenting particles. The important issue to be addressed here is whether droplet–turbulence interactions are modified by droplet sedimentation. For $\epsilon < 10 \text{ cm}^2 \text{ s}^{-3}$, $St < 0.2$ and Sv is significantly larger than one, then gravity dominates the motion of droplets and the inertia effect only introduces a weak modification to the motion.

3. Kinematic formulation of geometric collision kernel

In this paper, we shall neglect droplet–droplet aerodynamic interaction. In this case, the number of collisions per unit time is defined as *geometric* collision rate. Assuming that the volume concentration of droplets is small so the background airflow is not modified by the presence of droplets, droplet–droplet geometric collisions can be subdivided into combinations of bidisperse collisions involving two separate sizes and monodisperse collisions of nearly equal-size droplets. Furthermore, the monodisperse geometric collisions can be viewed as a limiting case of bidisperse collisions when the size ratio approaches one.

Now, consider a bidisperse system containing droplets of radii a_1 and a_2 ($a_2 < a_1$). The average geometric collision rate per unit volume, \dot{N}_c , in a large volume can be expressed as

$$\dot{N}_c = \Gamma_{12}^D n_1 n_2, \quad (6)$$

where n_1 and n_2 are average number concentrations of the two size groups and Γ_{12}^D is the average *dynamic* collision kernel.

The most general kinematic description of geometric collision [22, 32, 33] is given by

$$\Gamma_{12}^K = 2\pi R^2 \langle |w_r|(r=R) \rangle g_{12}(r=R), \quad (7)$$

where the radial relative velocity w_r is defined in terms of the relative velocity \mathbf{w} between two droplets with separation vector \mathbf{r} as $w_r \equiv \mathbf{w} \cdot \mathbf{r}/|\mathbf{r}|$, with $r \equiv |\mathbf{r}|$. The angle brackets $\langle \rangle$ denote

an average over all possible directions of \mathbf{r} in addition to the usual ensemble averaging or averaging over space and time for a homogeneous and stationary system. The average radial relative velocity at contact $\langle |w_r|(r = R) \rangle$ represents the average relative flux on the geometric collision sphere, a concept introduced initially by Saffman and Turner [20]. The other factor $g_{12}(r)$ in equation (7) is known as the RDF measuring the effect of preferential concentration on the pair number density at separation distance r . It is the ratio of the actual pair concentration to that in a uniform suspension. Thus, if the droplets are uniformly distributed in a volume, $g_{12}(r = R)$ is equal to unity. In DNS, g_{12} is computed, at any given time, as [33, 49]

$$g_{12}(r; t) = \frac{N_{\text{pairs}}/V_s}{N_1 N_2/V_B}, \quad (8)$$

where N_{pairs} is the total number of pairs detected with separation distance falling in a spherical shell of inner radius equal to $r_1 \equiv r - \delta_1$ and outer radius equal to $r_2 \equiv r + \delta_2$. Here, δ_1 and δ_2 are small fractions of r [31, 47]. V_s is the volume of the spherical shell, $V_s = 4\pi[(r + \delta_2)^3 - (r - \delta_1)^3]/3$. N_1 and N_2 are the total numbers of a_1 and a_2 droplets, respectively, used in the simulation, V_B is the computational domain size. Therefore, $n_1 = N_1/V_B$ and $n_2 = N_2/V_B \cdot g_{12}(r; t)$ is further averaged over time to obtain $g_{12}(r = R)$. Similarly, $\langle |w_r|(r = R) \rangle$ is computed based on the droplet pairs in the same spherical shell, by averaging the pair relative velocities over all pairs detected and over time.

The kinematic formulation has been validated against DNS dynamic collision kernel for both monodisperse and bidisperse collisions of non-sedimenting particles with no aerodynamic interactions [33, 49]. We will show in section 5.1 that this kinematic formulation is also valid for sedimenting inertial droplets although w_r and g_{12} are no longer spherically symmetric. The kinematic formulation implies that predicting the geometric collision kernel can be viewed alternatively as predicting the two kinematic properties $\langle |w_r| \rangle$ and g_{12} . Wang *et al* [34] have successfully extended the kinematic formulation to aerodynamically interacting droplets.

4. DNS

The numerical methods for simulating turbulent airflow and detecting droplet–droplet collisions have been described previously in [31, 34, 49, 56]. Consequently, only a brief description is presented below.

4.1. Turbulent flow field

A DNS of homogeneous isotropic turbulence was used to compute the air flow by a pseudo-spectral method. The incompressible Navier–Stokes and the continuity equations:

$$\frac{\partial \mathbf{U}}{\partial t} = \mathbf{U} \times \boldsymbol{\omega} - \nabla \left(\frac{P}{\rho} + \frac{1}{2} \mathbf{U}^2 \right) + \nu \nabla^2 \mathbf{U} + \mathbf{f}(x, t), \quad (9)$$

$$\nabla \cdot \mathbf{U} = 0, \quad (10)$$

were solved in a periodic cubic box. Here, $\boldsymbol{\omega}$ and P denote the fluid vorticity and pressure. The term $\mathbf{f}(x, t)$ is a random body force term, restricted to very low wavenumbers, that provides an energy source to sustain the air turbulence. Stationary turbulence can be reached since energy propagates from low to high wavenumbers; hence, the forcing energy propagates until viscous dissipation becomes active, establishing a quasi-steady energy balance. The time evolution was

computed using a second-order Adams–Bashforth scheme for the nonlinear terms and a second-order Crank–Nicholson scheme for the viscous term. The pressure was eliminated through the continuity equation.

The flow domain is discretized uniformly into N^3 grid points. This grid resolution determines the scale separation, and hence, the Reynolds number of the resulting flow. For this paper, we considered 32^3 , 64^3 and 128^3 grid points for each selected cloud-dissipation rate for a total of nine cases. Table 4 lists the flow parameters: the component rms fluctuating velocity u' , integral length scale L_f , fluid acceleration variance $\langle (Du/Dt)^2 \rangle$, longitudinal Taylor-type microscale of fluid acceleration λ_D , eddy turnover time T_e , Kolmogorov velocity scale v_k , Kolmogorov timescale τ_k , Kolmogorov length scale η , Taylor microscale λ , Taylor-microscale Reynolds number R_λ , size of the cubic box flow domain L_B , grid spacing Δx and flow time step size dt . The time step was chosen to ensure that the Courant–Friedrich–Levy (CFL) number was 0.3 or less for numerical stability and accuracy. The spatial resolution of the simulations were monitored by the value $k_{max}\eta$, which should be greater than unity for the smallest scales of flow to be resolved. Other details of the simulated flows can be found in [31].

It is important to note that, due to the limited scales in DNS, it may be possible that not all scales of motion affecting a droplet are resolved in DNS. To give an indication of this aspect, we list two scale ratios in table 4: The first is τ_p/T_e and the second is $\tau_p u'/L_B$, for $50\ \mu\text{m}$ droplets. The first ratio may be used to indicate the effect of unresolved large scales. The second ratio shows the influence of resolved large-eddy scales. Taking a value of 0.1 as a rough dividing line for the possible influence of a given large scale, we conclude that whereas the effect of unresolved large-scale motion may be neglected, the resolved large-scale motion does have some effect on larger droplets considered in this study, when the dissipation rate is high and the grid resolution is low. For all 128^3 , the scale ratios imply that all relevant scales of the fluid motion appear to have been resolved for the size range of droplets considered in this study. With increasing computing resources, we hope to address this aspect more systematically in the near future.

4.2. Motion of droplets

Since droplet–droplet aerodynamic interaction is not considered here, each droplet is treated as a point particle. The location and velocity of each droplet were advanced by integrating the equation of motion described in section 2.2, with a fourth-order, Adams–Moulton scheme for droplet velocity and a fourth-order, Adams–Bashforth scheme for droplet location. The fluid velocity at the droplet location was interpolated from the velocity values at the neighboring grid points using a six-point Lagrange interpolation. For most of the simulations, the Stokes drag was assumed. The effect of the nonlinear drag on our results will be discussed later in section 5.4.

The droplets were introduced into the flow when the air turbulence had reached the statistically stationary stage. The initial conditions were that the locations of the droplets were randomly distributed and the initial velocity was set equal to the local fluid velocity plus the terminal velocity of the droplet. After about $3 \times \max(\tau_{p1}, \tau_{p2})$, data on collision-related statistics were begun to be accumulated to obtain running averages, to minimize any effect of the initial conditions. To closely simulate the number density in clouds, typically of the order of 100 000 size-1 droplets and 100 000 size-2 droplets were followed. The same time step size was used to integrate the Navier–Stokes equation and the equation of motion for droplets. The time step must be made small compared to the droplet inertial response time and the flow Kolmogorov time. The proper choice of time step size has been discussed in detail in [56].

Table 4. DNS flow parameters and characteristics.

	$\epsilon = 10 \text{ cm}^2 \text{ s}^{-3}$			$\epsilon = 100 \text{ cm}^2 \text{ s}^{-3}$		
	32^3	64^3	128^3	32^3	64^3	128^3
u' (cm s ⁻¹)	2.805	3.806	4.937	4.987	6.768	8.779
L_f (cm)	2.224	5.547	12.164	1.251	3.119	6.839
$\langle (Du/Dt)^2 \rangle$ (cm ² s ⁻⁴)	0.720×10^2	1.184×10^2	1.582×10^2	2.281×10^3	3.752×10^3	5.010×10^3
λ_D (cm)	0.7404	0.8454	0.8912	0.4164	0.4754	0.5012
T_e (s)	0.787	1.449	2.434	0.248	0.458	0.771
v_k (cm s ⁻¹)	1.142	1.142	1.142	2.031	2.031	2.031
τ_k (s)	0.1304	0.1304	0.1304	0.0412	0.0412	0.0412
η (cm)	0.1488	0.1488	0.1488	0.0837	0.0837	0.0837
λ (cm)	1.416	1.922	2.493	0.796	1.081	1.402
R_λ	23.370	43.037	72.408	23.370	43.037	72.408
L_B (cm)	10.528	21.056	42.112	5.920	11.840	23.680
$\tau_p(50 \mu\text{m})/T_e$	0.042	0.023	0.013	0.132	0.071	0.093
$\tau_p(50 \mu\text{m})u'/L_B$	8.7×10^{-3}	5.9×10^{-3}	3.8×10^{-3}	2.8×10^{-2}	1.9×10^{-2}	1.2×10^{-2}
Δx (cm)	0.329	0.329	0.329	0.185	0.185	0.185
$dt \times 10^3$ (s)	4.568	3.515	2.843	1.443	1.110	0.898
CFL	0.2479	0.2831	0.301	0.2479	0.2831	0.301
$k_{\max}\eta$	1.2741	1.3619	1.3826	1.2741	1.3619	1.3826

	$\epsilon = 400 \text{ cm}^2 \text{ s}^{-3}$		
	32^3	64^3	128^3
u' (cm s ⁻¹)	7.054	9.572	12.416
L_f (cm)	0.884	2.206	4.837
$\langle (Du/Dt)^2 \rangle$ (cm ² s ⁻⁴)	1.825×10^4	3.002×10^4	4.008×10^4
λ_D (cm)	0.2944	0.3361	0.3544
T_e (s)	0.124	0.229	0.385
v_k (cm s ⁻¹)	2.872	2.872	2.872
τ_k (s)	0.0206	0.0206	0.0206
η (cm)	0.0592	0.0592	0.0592
λ (cm)	0.563	0.764	0.991
R_λ	23.370	43.037	72.408
L_B (cm)	4.192	8.384	16.768
$\tau_p(50 \mu\text{m})/T_e$	0.264	0.143	0.085
$\tau_p(50 \mu\text{m})u'/L_B$	5.5×10^{-2}	3.7×10^{-2}	2.4×10^{-2}
Δx (cm)	0.131	0.131	0.131
$dt \times 10^3$ (s)	0.722	0.555	0.449
CFL	0.2479	0.2831	0.301
$k_{\max}\eta$	1.2741	1.3619	1.3826

4.3. Collision detections and computation of kinematic properties

In the computation of the dynamic collision kernel, the collision events were detected during the simulation. The number of collisions was recorded in each time step. The mean and statistical uncertainty of the dynamic collision kernel were evaluated by using the values recorded for a

large number of time steps. The method for collision detection went through several iterations and the final version utilized the efficient cell-index method and the concept of linked lists [57]. Since the geometric collision is of interest here, the droplets were allowed to overlap at the beginning of a time step and were not removed at all from the system after collision. A collision detection grid was carefully chosen so that all collision events were counted and, at the same time, no time was wasted on processing pairs with large separations. Once the rate of collision per unit volume \dot{N}_c is computed, the dynamic collision kernel Γ_{12}^D can be determined from equation (6). While we were primarily interested in the 1–2 collision events, same-size collisions (1–1 and 2–2) were also counted.

For a given time duration T and the volume V_B of the computational domain, the number of droplets determines the number of pairs and the total collision rate. A larger number of droplets lead to a larger number of collisions and smaller statistical errors. It can be shown that the relative uncertainty of the computed dynamic collision kernel can be roughly estimated as [56, 58]

$$\left[\left(\frac{V_B}{\Gamma_{12}^D T} - 1 \right) / N_{\text{pairs}} \right]^{1/2}, \quad (11)$$

where $N_{\text{pairs}} = N_{p_1} N_{p_2}$. This was used to monitor the relative uncertainty of the resulting dynamic collision kernel. The time interval T was typically around 10 eddy turnover times. The relative uncertainty may be further reduced by averaging over several independent runs of the same parameter setting, but different initial flow or particle realizations.

A separate code was used to independently compute the kinematic properties $\langle |w_r(r)| \rangle$ and $g_{12}(r)$. They were computed, at an instant of time, using all the pairs with interparticle distance r falling between $(R - \delta/2)$ and $(R + \delta/2)$, where δ is a small fraction of R . Wang *et al* [33] found that a suitable value for δ should be about $0.02R$ or less. We used a value of $\delta = 0.02R$. The velocities and the separation vectors of all detected pairs were recorded during the simulations at different times and were used to obtain $g_{12}(r = R)$, using equations (8), and the radial relative velocity by $\langle |w_r| \rangle = \langle |v_r^{(2)} - v_r^{(1)}| \rangle$, where $v_r^{(2)}$ and $v_r^{(1)}$ are the velocity components of the droplets along the axis defined by the separation vector. Again the mean and statistical uncertainty of $\langle |w_r(r = R)| \rangle$ and $g_{12}(r = R)$ were evaluated using their values at different times. For further details on collision detections and computation of kinematic properties, the readers are referred to Zhou *et al* [49, 59].

Since we considered geometric collisions, droplets were allowed to overlap and move independently. Namely, they were treated as ghost particles. Although somewhat unrealistic, this treatment maintains the statistical stationarity of the system, and it is consistent with the Saffman and Turner formulation [20, 60]. Additionally, the RDF at contact can be calculated more accurately using this treatment. We had compared the collision kernel for ghost particles with the collision kernel base on non-overlapping droplets [34], the results were very similar.

5. Results

5.1. Validation of the kinematic kernel against the dynamic kernel

Before presenting results for turbulent geometric collision, we shall first demonstrate that the kinematic formulation, equation (7), is consistent with the dynamic formulation, equation (6),

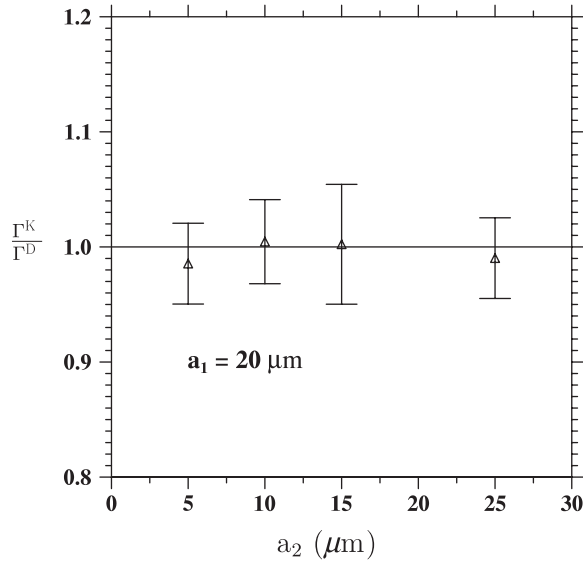


Figure 2. Ratio of DNS kinematic collision kernel to DNS dynamic collision kernel for gravitational collision in stagnant air.

for droplets settling under gravity in a turbulent flow. The gravity introduces a dependence of the relative motion on the orientation of the separation and breaks the spherical symmetry of pair statistics.

In figure 2, we compare the dynamic collision kernel with the kinematic collision kernel for collisions of $20 \mu\text{m}$ droplets with droplets of different sizes in stagnant air. The two methods of obtaining the collision kernel can be shown theoretically to give identical results for this simple case [22]. The numerical results contain statistical uncertainties, but otherwise confirm that the kinematic formulation is consistent with dynamic collision detections. For this simplest case, this consistency test was undertaken mainly to validate the DNS code.

The radial relative velocity and the RDF for the above test cases in stagnant air are shown in figure 3. The numerical results agree, within statistical uncertainties, with the theoretical values given by

$$\langle |w_r|(r=R) \rangle = \frac{1}{2}|v_{p_2} - v_{p_1}|, \quad g_{12}(r=R) = 1.0, \quad \Gamma_{12}^K = \pi R^2 |v_{p_2} - v_{p_1}|. \quad (12)$$

These results validate the code implementation of the kinematic properties.

A more interesting comparison would be for sedimenting cloud droplets in turbulent air. Figure 4 compares the collision kernel results from the two formulations at two levels of flow dissipation rate. Clearly, the kinematic collision kernel agrees with the dynamic collision kernel at both intensities of turbulence. In DNS, the kinematic properties can be more easily obtained than the dynamic collision kernel as more droplet pairs can be used to compute the kinematic properties [59]. The results here confirm that the kinematic formulation can be used to predict the collision kernel for sedimenting inertial droplets in a turbulent flow, although the kinematic properties w_r and g_{12} are no longer spherically symmetric. The same conclusion was reached in [50, 34].

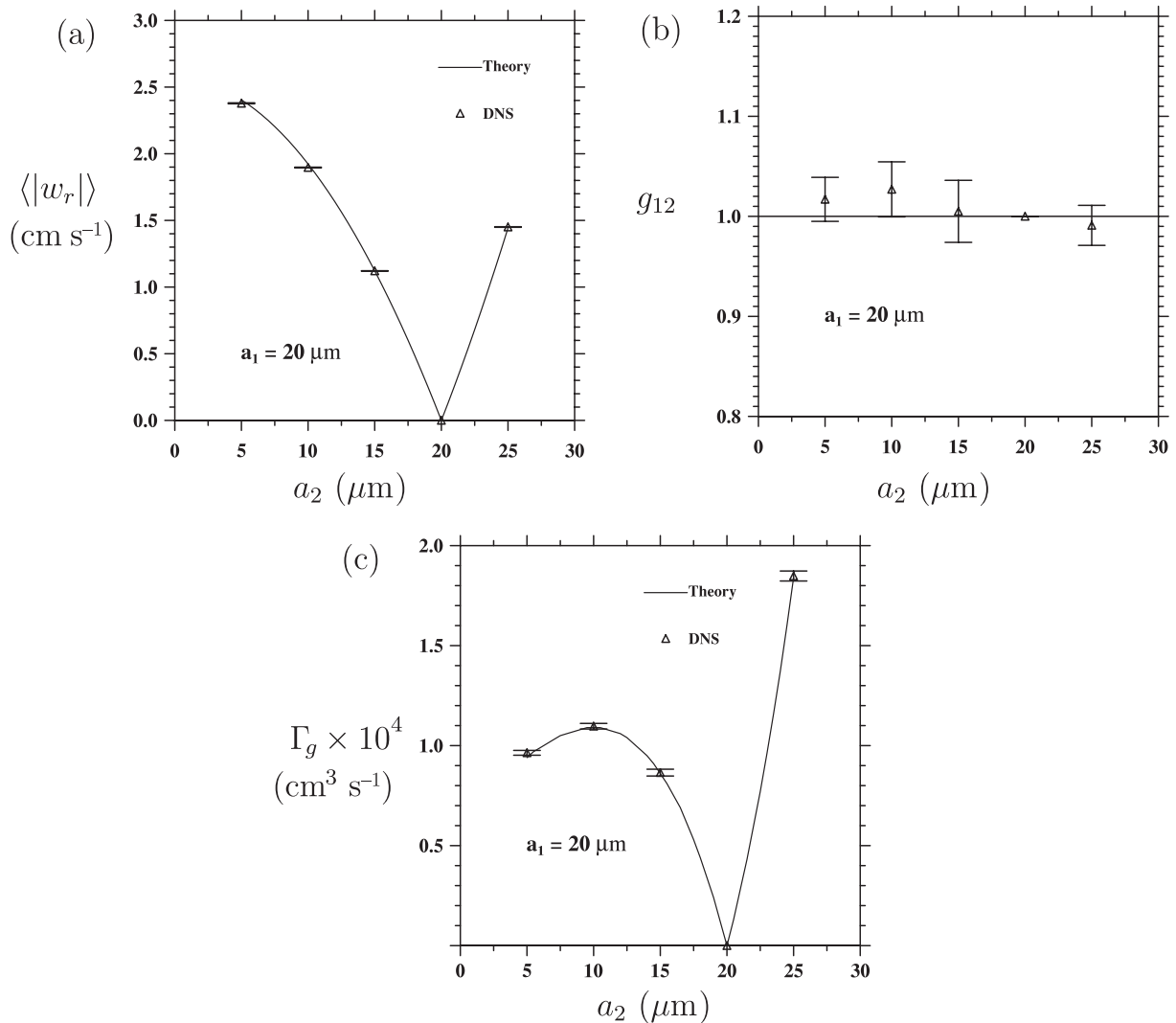


Figure 3. Comparison of DNS results with the theory for droplets settling in stagnant air: (a) $\langle |w_r| \rangle$, (b) g_{12} and (c) Γ_{12} .

5.2. Geometric collision kernel and related kinematic properties

DNS results of geometric collision kernel, in cm³ s⁻¹, are tabulated in table 5 for three different flow dissipation rates. For each flow dissipation rate, three flow Reynolds numbers were considered. Twenty-one droplet size combinations were simulated, 6 for monodisperse collisions and 15 for bidisperse collisions. The values in parentheses represent estimated standard deviation of the kernel, which is typically two orders of magnitude smaller than the obtained kernel. Two interesting observations can be made here. Firstly, for a given bidisperse size combination, the collision kernel increases with the flow dissipation rate, as a result of increasing effect of air turbulence on the motion of droplets. The effect of flow Reynolds number is relatively weak and somewhat mixed: for some cases, the kernel is slightly larger for larger R_λ , and for other cases, the kernel is slightly less for larger R_λ . This supports our working assumption that the dissipation-range turbulent motion governs the collision process

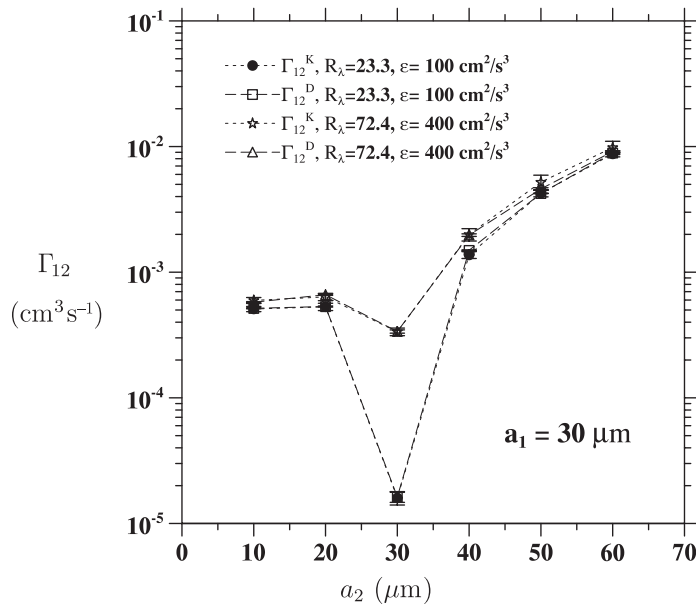


Figure 4. Comparison of the kinematic collision kernel and the dynamic collision kernel for sedimenting droplets in turbulent air.

so that the flow dissipation rate plays a primary role and the flow Reynolds number plays a secondary role as far as geometric collision of small cloud droplets (say, $<20 \mu\text{m}$) is concerned. Secondly, for a monodisperse system, the gravitational kernel vanishes, but the collision kernel in a turbulent flow is nonzero. In this case, the resulting kernel, although relatively small in magnitude, depends much more strongly on both the flow dissipation rate and R_λ . This turbulent collision among nearly equal sized droplets should be carefully considered, in view of the narrow droplet size distribution typically generated by condensational growth. This turbulent collision mechanism has been shown to play a role in shortening the time for the initial phase (i.e. autoconversion phase) of the growth process by collision–coalescence [56].

The ratio of the turbulent collision kernel to the gravitational kernel is shown in table 6 for all bidisperse interactions. This represents the overall enhancement of *geometric* collision rate by air turbulence. This enhancement depends mainly on the magnitude of flow dissipation rate, from just a few percent for weak turbulence with $\epsilon = 10 \text{ cm}^2 \text{ s}^{-3}$ up to 47% for strong cloud turbulence with $\epsilon = 400 \text{ cm}^2 \text{ s}^{-3}$. It also increases with the droplet size as the inertial effect becomes more important in altering the motion and distribution of droplets. The highlighted cells in the table indicate values that are larger than 1.1. For the case of $\epsilon = 10 \text{ cm}^2 \text{ s}^{-3}$, the relative enhancement is very small and numerical uncertainties can lead to an average ratio slightly less than one. For the two size combinations (40 and $50 \mu\text{m}$) and (50 and $60 \mu\text{m}$) shown in the table, we note that the ratio decreases with increasing flow Reynolds number. This could be due to the inadequate resolution of large-scale motion for these larger droplets, as stated in section 4.1, these data should be re-examined in future with higher resolution DNS.

According to the kinematic formulation, this enhancement may be decomposed into two parts: the effect of turbulence on enhancing the radial relative motion (the turbulent transport effect, table 7) and that on the RDF (the accumulation effect, table 8). Take, for example, the case of $a_1 = 10 \mu\text{m}$ and $a_2 = 20 \mu\text{m}$ in a flow with $\epsilon = 400 \text{ cm}^2 \text{ s}^{-3}$ and $R_\lambda = 72.4$, the

Table 5. DNS results of dynamic collision kernel ($\text{cm}^3 \text{s}^{-1}$).

a_1	a_2	$10 \text{ cm}^2 \text{ s}^{-3}$			$100 \text{ cm}^2 \text{ s}^{-3}$			$400 \text{ cm}^2 \text{ s}^{-3}$		
		$R_\lambda = 23.4$	$R_\lambda = 43.0$	$R_\lambda = 72.4$	$R_\lambda = 23.4$	$R_\lambda = 43.0$	$R_\lambda = 72.4$	$R_\lambda = 23.4$	$R_\lambda = 43.0$	$R_\lambda = 72.4$
10	10	4.026E-07 (2.31E-07)	0.000E+00 (0.00E+00)	0.000E+00 (0.00E+00)	4.792E-07 (1.72E-07)	3.416E-07 (1.80E-07)	5.061E-07 (2.24E-07)	7.936E-07 (1.99E-07)	8.206E-07 (2.72E-07)	5.741E-07 (1.94E-07)
10	20	1.094E-04 (1.57E-06)	1.100E-04 (1.69E-06)	1.151E-04 (4.01E-06)	1.126E-04 (1.16E-06)	1.122E-04 (1.52E-06)	1.154E-04 (2.11E-06)	1.164E-04 (1.15E-06)	1.235E-04 (1.38E-06)	1.245E-04 (1.75E-06)
10	30	5.066E-04 (4.31E-06)	5.197E-04 (4.96E-06)	5.018E-04 (1.303E-05)	5.228E-04 (1.85E-06)	5.292E-04 (2.31E-06)	5.278E-04 (6.77E-06)	5.456E-04 (1.16E-06)	5.60E-04 (1.39E-06)	5.707E-04 (4.10E-06)
10	40	1.509E-03 (1.43E-05)	1.537E-03 (1.65E-05)	1.573E-03 (4.33E-05)	1.534E-03 (8.28E-06)	1.541E-03 (1.70E-05)	1.520E-03 (1.75E-05)	1.591E-03 (7.73E-06)	1.637E-03 (1.70E-05)	1.647E-03 (1.98E-05)
10	50	3.509E-03 (2.86E-05)	3.504E-03 (4.96E-05)	3.548E-03 (3.46E-05)	3.551E-03 (7.62E-05)	3.545E-03 (3.34E-05)	3.596E-03 (3.65E-05)	3.610E-03 (2.06E-05)	3.642E-03 (3.35E-05)	3.725E-03 (3.18E-05)
10	60	6.956E-03 (6.35E-05)	6.965E-03 (6.42E-05)	7.076E-03 (1.27E-04)	6.954E-03 (2.34E-05)	7.036E-03 (6.46E-05)	7.046E-03 (7.52E-05)	7.047E-03 (1.48E-05)	7.103E-03 (4.91E-05)	7.274E-03 (8.28E-05)
20	20	9.584E-07 (3.48E-07)	1.413E-06 (3.33E-07)	1.295E-06 (9.11E-07)	2.639E-06 (3.49E-07)	4.691E-06 (6.13E-07)	5.154E-06 (8.43E-07)	1.405E-05 (7.73E-07)	2.216E-05 (1.33E-06)	2.561E-05 (1.69E-06)
20	30	5.119E-04 (5.71E-06)	4.998E-04 (5.29E-06)	4.854E-04 (1.03E-05)	5.329E-04 (5.77E-06)	5.387E-04 (5.77E-06)	5.420E-04 (7.58E-06)	5.900E-04 (5.86E-06)	6.360E-04 (8.33E-06)	6.617E-04 (7.72E-06)
20	40	1.714E-03 (1.55E-05)	1.725E-03 (1.78E-05)	1.768E-03 (2.63E-05)	1.807E-03 (1.88E-05)	1.819E-03 (1.94E-05)	1.810E-03 (1.94E-05)	1.846E-03 (1.10E-05)	1.961E-03 (2.65E-05)	1.954E-03 (3.18E-05)
20	50	4.194E-03 (3.44E-05)	4.147E-03 (3.95E-05)	4.068E-03 (7.61E-05)	4.197E-03 (1.87E-05)	4.252E-03 (4.05E-05)	4.196E-03 (5.24E-05)	4.266E-03 (2.11E-05)	4.341E-03 (4.40E-05)	4.429E-03 (5.69E-05)
20	60	8.333E-03 (6.63E-05)	8.251E-03 (5.56E-05)	8.228E-03 (1.44E-04)	8.307E-03 (2.70E-05)	8.295E-03 (7.41E-05)	8.302E-03 (1.01E-04)	8.358E-03 (2.70E-05)	8.496E-03 (6.65E-05)	8.595E-03 (1.09E-04)
30	30	2.475E-06 (6.29E-07)	3.785E-06 (8.77E-07)	2.479E-06 (1.49E-06)	1.624E-05 (1.52E-06)	2.559E-05 (2.26E-06)	3.023E-05 (3.75E-06)	1.514E-04 (4.51E-06)	2.715E-04 (8.44E-06)	3.372E-04 (1.01E-05)
30	40	1.414E-03 (1.59E-05)	1.398E-03 (1.49E-05)	1.391E-03 (2.30E-05)	1.494E-03 (1.24E-05)	1.517E-03 (2.33E-05)	1.540E-03 (2.13E-05)	1.658E-03 (1.50E-05)	1.802E-03 (2.97E-05)	1.972E-03 (4.67E-05)
30	50	4.160E-03 (3.21E-05)	4.116E-03 (4.22E-05)	4.077E-03 (5.06E-05)	4.238E-03 (2.43E-05)	4.405E-03 (5.41E-05)	4.287E-03 (6.72E-05)	4.494E-03 (2.34E-05)	4.612E-03 (4.82E-05)	4.600E-03 (1.01E-04)
30	60	8.772E-03 (7.35E-05)	8.862E-03 (8.64E-05)	8.655E-03 (9.87E-05)	8.893E-03 (3.43E-05)	9.117E-03 (7.75E-05)	8.668E-03 (1.45E-04)	9.342E-03 (3.73E-05)	9.308E-03 (6.72E-05)	9.134E-03 (1.30E-04)
40	40	5.503E-06 (1.30E-06)	4.239E-06 (1.40E-06)	1.033E-05 (3.79E-06)	5.274E-05 (3.05E-06)	1.095E-04 (6.95E-06)	1.475E-04 (1.01E-05)	3.678E-04 (9.44E-06)	6.862E-04 (2.24E-05)	9.065E-04 (2.71E-05)
40	50	3.132E-03 (2.71E-05)	3.051E-03 (3.31E-05)	2.976E-03 (4.41E-05)	3.424E-03 (2.20E-05)	3.400E-03 (4.92E-05)	3.345E-03 (7.77E-05)	3.596E-03 (2.25E-05)	3.767E-03 (4.66E-05)	3.853E-03 (9.26E-05)
40	60	8.207E-03 (7.37E-05)	8.173E-03 (8.06E-05)	8.182E-03 (9.70E-05)	8.796E-03 (3.99E-05)	8.632E-03 (8.07E-05)	8.326E-03 (1.85E-04)	8.971E-03 (3.91E-05)	9.013E-03 (7.50E-05)	9.124E-03 (1.48E-04)
50	50	7.130E-06 (1.94E-06)	1.174E-05 (3.25E-06)	1.853E-05 (6.63E-06)	6.507E-05 (4.24E-06)	2.061E-04 (1.49E-05)	3.263E-04 (2.25E-05)	4.192E-04 (1.26E-05)	9.509E-04 (3.46E-05)	1.388E-03 (5.32E-05)
50	60	5.894E-03 (5.66E-05)	5.991E-03 (7.74E-05)	5.630E-03 (8.39E-05)	7.195E-03 (5.22E-05)	6.645E-03 (7.21E-05)	6.027E-03 (1.43E-04)	7.860E-03 (6.22E-05)	7.139E-03 (6.02E-05)	6.904E-03 (1.25E-04)
60	60	1.340E-05 (4.96E-06)	1.473E-05 (4.76E-06)	2.819E-05 (1.00E-05)	8.118E-05 (4.39E-06)	2.005E-04 (1.69E-05)	4.005E-04 (3.53E-05)	5.174E-04 (1.78E-05)	9.116E-04 (3.32E-05)	1.635E-03 (6.45E-05)

overall enhancement is 14.5%. Tables 7 and 8 show that roughly 10% of this is due to the turbulent transport effect, and the remaining 4% is due to the accumulation effect. For a second case of $a_1 = 20 \mu\text{m}$ and $a_2 = 30 \mu\text{m}$ in the same flow, the overall enhancement of 31.4% is roughly equally shared by the turbulent transport effect and the accumulation effect. Therefore, the turbulent transport effect dominates the enhancement for smaller cloud droplets, while the accumulation effect could become equally important for larger cloud droplets. Another important observation from table 8 is that the accumulation effect quickly diminishes as the sizes of the colliding droplets become different (see also figure 9 below). Again, values larger than 1.1 in table 8 are highlighted. Numerical uncertainties for some of the cases are larger

Table 6. The ratio of turbulent collision kernel to gravitational geometric collision kernel. The values in parentheses are the corresponding statistical uncertainties (\pm one standard deviation).

a_1 (μm)	a_2 (μm)	ϵ								
		$10 \text{ cm}^2 \text{ s}^{-3}$			$100 \text{ cm}^2 \text{ s}^{-3}$			$400 \text{ cm}^2 \text{ s}^{-3}$		
		R_λ			R_λ			R_λ		
		23.4	43.0	72.4	23.4	43.0	72.4	23.4	43.0	72.4
10	20	1.006 (0.014)	1.011 (0.016)	1.058 (0.037)	1.035 (0.011)	1.031 (0.014)	1.061 (0.019)	1.070 (0.011)	1.136 (0.013)	1.145 (0.016)
10	30	0.988 (0.008)	1.013 (0.010)	0.978 (0.025)	1.019 (0.004)	1.032 (0.004)	1.029 (0.013)	1.064 (0.002)	1.092 (0.003)	1.113 (0.008)
10	40	0.999 (0.009)	1.018 (0.010)	1.041 (0.029)	1.016 (0.005)	1.020 (0.011)	1.006 (0.012)	1.053 (0.005)	1.083 (0.011)	1.090 (0.013)
10	50	1.008 (0.008)	1.007 (0.010)	1.019 (0.022)	1.020 (0.005)	1.018 (0.010)	1.033 (0.010)	1.037 (0.006)	1.046 (0.010)	1.070 (0.011)
10	60	1.007 (0.009)	1.008 (0.009)	1.024 (0.018)	1.007 (0.003)	1.018 (0.009)	1.020 (0.011)	1.020 (0.002)	1.028 (0.007)	1.053 (0.012)
20	30	1.016 (0.011)	0.992 (0.011)	0.964 (0.020)	1.058 (0.011)	1.070 (0.011)	1.076 (0.015)	1.172 (0.012)	1.263 (0.017)	1.314 (0.015)
20	40	0.985 (0.009)	0.991 (0.010)	1.016 (0.015)	1.038 (0.008)	1.045 (0.011)	1.040 (0.011)	1.061 (0.006)	1.127 (0.015)	1.123 (0.018)
20	50	1.012 (0.008)	1.000 (0.010)	0.981 (0.018)	1.013 (0.005)	1.026 (0.010)	1.012 (0.013)	1.029 (0.005)	1.047 (0.011)	1.068 (0.014)
20	60	1.010 (0.008)	1.000 (0.007)	0.997 (0.017)	1.007 (0.003)	1.005 (0.009)	1.006 (0.012)	1.013 (0.003)	1.030 (0.008)	1.042 (0.013)
30	40	1.023 (0.011)	1.012 (0.011)	1.007 (0.017)	1.081 (0.009)	1.098 (0.017)	1.115 (0.015)	1.200 (0.011)	1.304 (0.021)	1.427 (0.034)
30	50	1.008 (0.008)	0.998 (0.010)	0.988 (0.012)	1.027 (0.006)	1.068 (0.013)	1.039 (0.016)	1.089 (0.006)	1.118 (0.012)	1.115 (0.024)
30	60	0.996 (0.008)	1.006 (0.010)	0.982 (0.011)	1.009 (0.004)	1.035 (0.009)	0.984 (0.016)	1.060 (0.004)	1.056 (0.008)	1.037 (0.015)
40	50	1.067 (0.009)	1.039 (0.011)	1.013 (0.015)	1.166 (0.007)	1.158 (0.017)	1.139 (0.026)	1.225 (0.008)	1.283 (0.016)	1.312 (0.032)
40	60	1.019 (0.009)	1.014 (0.010)	1.016 (0.012)	1.092 (0.005)	1.071 (0.010)	1.033 (0.023)	1.113 (0.005)	1.119 (0.009)	1.132 (0.018)
50	60	1.099 (0.011)	1.117 (0.014)	1.050 (0.016)	1.342 (0.010)	1.239 (0.013)	1.124 (0.027)	1.466 (0.012)	1.331 (0.011)	1.288 (0.023)

due to the limited computing resources. High-resolution DNS using message passing interface (MPI) are under development, which will address this aspect in the near future.

For the case of monodisperse interactions, however, the accumulation effect can dominate the collision kernel. The RDF can be of the order of 10 or larger for high flow dissipation rates (table 8).

Tables 5 through 8 represent a compilation of DNS results covering the largest combinations of relevant parameters for sedimenting cloud droplets. They together extend the DNS data published previously in [34, 50, 51] for sedimenting droplets.

In very recent studies, Franklin *et al* [51] compiled results for the radius ranging from 10 to 30 μm and a dissipation rate ranging from 95 to 1535 $\text{cm}^2 \text{ s}^{-3}$. In figure 5, we compare

Table 7. DNS results of $\langle |w_r| \rangle$ (cm s^{-1}). The values in the parentheses are the corresponding statistical uncertainties (\pm one standard deviation).

a_1 (μm)	a_2 (μm)	Gravity only	ϵ								
			$10 \text{ cm}^2 \text{ s}^{-3}$			$100 \text{ cm}^2 \text{ s}^{-3}$			$400 \text{ cm}^2 \text{ s}^{-3}$		
			R_λ			R_λ			R_λ		
23.4	43.0	72.4	23.4	43.0	72.4	23.4	43.0	72.4			
10	10	0.0	0.0042 (0.0001)	0.0000 (0.0000)	0.0000 (0.0000)	0.0083 (0.0004)	0.0104 (0.0007)	0.0120 (0.0012)	0.0246 (0.0008)	0.0206 (0.0012)	0.0247 (0.0020)
10	20	1.923	1.9026 (0.0314)	1.2303 (0.0411)	1.8927 (0.0843)	1.9601 (0.0239)	1.8768 (0.0294)	2.0240 (0.0519)	1.9460 (0.0231)	2.0081 (0.0312)	2.1013 (0.0372)
10	30	5.129	5.2215 (0.0706)	5.2086 (0.0806)	5.2245 (0.2290)	5.2001 (0.0309)	5.2300 (0.0385)	5.3156 (0.1130)	5.4314 (0.0200)	5.4393 (0.0251)	5.4771 (0.0708)
10	40	9.617	9.5720 (0.1896)	9.8049 (0.2055)	9.4186 (0.5925)	9.7991 (0.1183)	9.9554 (0.2061)	9.6236 (0.2312)	9.9498 (0.1042)	10.3605 (0.2380)	10.3614 (0.2673)
10	50	15.388	15.4243 (0.3078)	15.3117 (0.3658)	16.1403 (0.7821)	15.3078 (0.1908)	15.7826 (0.3521)	15.8227 (0.3839)	15.7347 (0.2000)	15.9450 (0.3858)	16.4044 (0.4477)
10	60	22.441	22.6362 (0.4734)	23.5599 (0.5228)	24.3773 (1.1193)	22.5954 (0.2193)	23.4653 (0.5893)	22.9248 (0.7111)	22.9298 (0.1106)	23.4133 (0.4407)	23.9669 (0.7152)
20	20	0.0	0.0052 (0.0004)	0.0080 (0.0008)	0.0143 (0.0102)	0.0225 (0.0003)	0.0223 (0.0008)	0.0295 (0.0038)	0.0430 (0.0007)	0.0414 (0.0008)	0.0487 (0.0010)
20	30	3.205	3.2580 (0.0769)	3.1792 (0.0755)	2.9678 (0.1672)	3.2569 (0.0759)	3.3279 (0.0450)	3.3088 (0.0989)	3.6000 (0.0838)	3.6151 (0.0959)	3.5979 (0.0893)
20	40	7.694	7.2993 (0.2260)	8.2027 (0.2550)	6.5537 (0.3676)	7.9654 (0.1859)	7.8431 (0.2653)	8.0923 (0.3200)	8.4753 (0.1536)	8.7605 (0.3189)	8.3664 (0.3286)
20	50	13.464	12.9898 (0.3990)	13.7363 (0.5306)	13.0868 (1.0297)	13.8613 (0.2443)	14.1471 (0.5106)	13.8796 (0.6819)	14.0495 (0.2492)	14.5866 (0.4872)	14.4914 (0.5538)
20	60	20.517	20.1635 (0.8036)	20.5985 (0.6303)	20.7621 (1.6073)	20.9189 (0.3188)	20.1444 (0.7952)	21.5174 (1.3291)	20.8684 (0.2850)	20.6940 (0.5861)	20.8566 (0.8886)
30	30	0.0	0.0082 (0.0009)	0.0105 (0.0014)	0.0110 (0.0142)	0.0305 (0.0012)	0.0314 (0.0006)	0.0323 (0.0021)	0.0801 (0.0018)	0.0923 (0.0027)	0.0882 (0.0030)
30	40	4.488	4.6746 (0.1906)	4.1913 (0.1756)	4.6287 (0.2342)	4.5491 (0.1122)	4.9338 (0.1939)	4.8052 (0.1820)	5.1519 (0.0932)	5.8088 (0.2135)	5.8182 (0.2579)
30	50	10.258	10.2177 (0.3910)	10.4476 (0.5009)	10.4197 (0.6706)	10.6381 (0.2436)	11.3064 (0.4580)	9.9614 (0.5150)	10.6990 (0.1557)	11.2457 (0.3074)	11.8929 (0.5586)
30	60	17.311	16.3535 (0.9852)	16.3066 (1.0879)	16.4510 (1.1156)	17.7121 (0.3389)	17.7448 (0.6794)	17.0378 (1.2148)	17.7799 (0.2116)	18.1798 (0.4203)	19.3753 (0.8606)
40	40	0.0	0.0115 (0.0010)	0.0131 (0.0053)	0.0104 (0.0057)	0.0338 (0.0007)	0.0387 (0.0013)	0.0435 (0.0028)	0.1008 (0.0020)	0.1217 (0.0047)	0.1427 (0.0057)
40	50	5.770	5.5903 (0.2324)	5.4857 (0.3207)	6.1128 (0.3092)	5.9287 (0.1082)	6.2618 (0.2179)	6.0141 (0.3105)	6.1100 (0.0681)	6.8143 (0.1601)	7.1730 (0.3406)
40	60	12.823	12.3016 (0.7504)	12.7379 (0.8553)	13.1884 (0.7415)	13.1010 (0.2028)	13.2056 (0.4299)	12.7466 (0.9086)	13.3519 (0.1294)	13.4474 (0.2595)	14.8824 (0.5643)
50	50	0.0	0.0118 (0.0044)	0.0115 (0.0038)	0.0162 (0.0110)	0.0326 (0.0007)	0.0412 (0.0016)	0.0444 (0.0023)	0.0869 (0.0013)	0.1172 (0.0038)	0.1537 (0.0078)
50	60	7.0529	7.4904 (0.3394)	6.6426 (0.3470)	7.5736 (0.4029)	7.0420 (0.0872)	7.3359 (0.1843)	7.2318 (0.4323)	7.2111 (0.0319)	7.3769 (0.1173)	7.9946 (0.2811)
60	60	0.0	0.0095 (0.0066)	0.0112 (0.0050)	0.0133 (0.0065)	0.0318 (0.0005)	0.0361 (0.0011)	0.0430 (0.0029)	0.0974 (0.0009)	0.1020 (0.0022)	0.1304 (0.0050)

our results with theirs for the case of $a_1 = 30 \mu\text{m}$ and $a_2 = 10 \mu\text{m}$. It is noted that, in the work of Franklin *et al* [51], the dissipation rate and flow Reynolds number were not independently varied. The four flow dissipation rates of 95, 280, 656 and $1535 \text{ cm}^2 \text{ s}^{-3}$ used in their work correspond to the four flow Taylor-microscale Reynolds numbers of 33, 40, 48 and 55, respectively, while in our DNS, the dissipation rate and flow Reynolds number were independently varied. Figure 5 shows that our results are in reasonable agreement with those

Table 8. DNS results of g_{12} . The values in the parentheses are the corresponding statistical uncertainties (\pm one standard deviation).

a_1 (μm)	a_2 (μm)	ϵ								
		$10 \text{ cm}^2 \text{ s}^{-3}$			$100 \text{ cm}^2 \text{ s}^{-3}$			$400 \text{ cm}^2 \text{ s}^{-3}$		
		R_λ			R_λ			R_λ		
		23.4	43.0	72.4	23.4	43.0	72.4	23.4	43.0	72.4
10	10	1.488 (0.352)	1.000 (0.000)	1.000 (0.000)	1.562 (0.411)	0.953 (0.405)	1.433 (0.630)	1.213 (0.232)	1.639 (0.432)	0.945 (0.252)
10	20	1.026 (0.029)	1.006 (0.033)	0.945 (0.076)	1.041 (0.024)	1.042 (0.026)	1.104 (0.054)	1.060 (0.021)	1.076 (0.031)	1.043 (0.033)
10	30	0.973 (0.024)	1.000 (0.028)	0.987 (0.078)	0.997 (0.010)	1.010 (0.013)	1.010 (0.037)	1.012 (0.006)	1.015 (0.008)	1.040 (0.021)
10	40	1.015 (0.034)	1.004 (0.039)	1.010 (0.104)	1.010 (0.022)	0.986 (0.033)	0.944 (0.036)	1.009 (0.017)	1.047 (0.040)	1.047 (0.044)
10	50	0.977 (0.031)	0.984 (0.044)	1.122 (0.097)	1.019 (0.021)	1.033 (0.038)	1.045 (0.042)	0.975 (0.022)	0.994 (0.039)	1.045 (0.049)
10	60	0.994 (0.039)	1.063 (0.044)	1.038 (0.003)	0.991 (0.017)	0.968 (0.046)	0.974 (0.050)	0.995 (0.008)	1.005 (0.031)	1.019 (0.044)
20	20	1.552 (0.310)	1.067 (0.202)	1.407 (0.571)	1.209 (0.103)	1.936 (0.231)	1.814 (0.193)	3.179 (0.157)	5.032 (0.324)	5.087 (0.332)
20	30	1.054 (0.046)	0.985 (0.042)	0.971 (0.093)	1.037 (0.044)	1.003 (0.022)	1.024 (0.051)	1.032 (0.041)	1.127 (0.043)	1.125 (0.046)
20	40	0.999 (0.050)	1.002 (0.056)	0.884 (0.081)	1.071 (0.042)	0.930 (0.051)	0.974 (0.058)	1.004 (0.029)	1.018 (0.052)	1.038 (0.057)
20	50	1.046 (0.053)	0.946 (0.066)	0.991 (0.135)	1.081 (0.033)	0.984 (0.057)	0.985 (0.085)	0.970 (0.027)	1.087 (0.056)	1.048 (0.063)
20	60	1.139 (0.079)	1.091 (0.059)	1.055 (0.140)	1.028 (0.026)	1.006 (0.068)	1.001 (0.097)	1.007 (0.021)	1.057 (0.045)	0.959 (0.077)
30	30	1.671 (0.331)	1.382 (0.248)	0.879 (0.356)	2.313 (0.183)	3.854 (0.295)	3.227 (0.493)	8.184 (0.240)	13.256 (0.406)	16.824 (0.591)
30	40	0.881 (0.060)	0.927 (0.065)	1.222 (0.108)	0.979 (0.036)	1.024 (0.069)	0.979 (0.059)	1.108 (0.032)	1.053 (0.057)	1.114 (0.073)
30	50	0.969 (0.063)	1.030 (0.086)	1.077 (0.118)	0.993 (0.040)	1.073 (0.081)	0.934 (0.074)	1.024 (0.022)	1.048 (0.048)	1.089 (0.092)
30	60	1.020 (0.098)	0.915 (0.100)	1.018 (0.116)	0.969 (0.032)	0.993 (0.067)	1.054 (0.112)	0.989 (0.018)	1.011 (0.039)	0.996 (0.073)
40	40	1.284 (0.240)	0.916 (0.235)	2.240 (0.534)	3.690 (0.192)	7.163 (0.476)	7.913 (0.549)	8.701 (0.252)	14.019 (0.550)	15.711 (0.641)
40	50	1.144 (0.074)	0.962 (0.085)	0.939 (0.085)	1.179 (0.033)	1.244 (0.070)	1.206 (0.108)	1.168 (0.021)	1.132 (0.038)	0.984 (0.077)
40	60	1.019 (0.105)	0.992 (0.111)	1.267 (0.140)	1.089 (0.030)	1.057 (0.059)	1.051 (0.120)	1.063 (0.017)	1.061 (0.035)	0.997 (0.064)
50	50	0.892 (0.207)	1.577 (0.342)	2.526 (0.554)	2.974 (0.158)	8.006 (0.524)	10.781 (0.760)	7.254 (0.211)	12.180 (0.470)	14.491 (0.720)
50	60	1.112 (0.093)	1.214 (0.091)	1.016 (0.103)	1.330 (0.028)	1.250 (0.056)	0.959 (0.093)	1.429 (0.014)	1.230 (0.035)	1.191 (0.060)
60	60	1.194 (0.274)	1.268 (0.258)	2.568 (0.543)	2.733 (0.105)	5.812 (0.441)	9.566 (0.802)	5.647 (0.153)	9.373 (0.360)	13.721 (0.689)

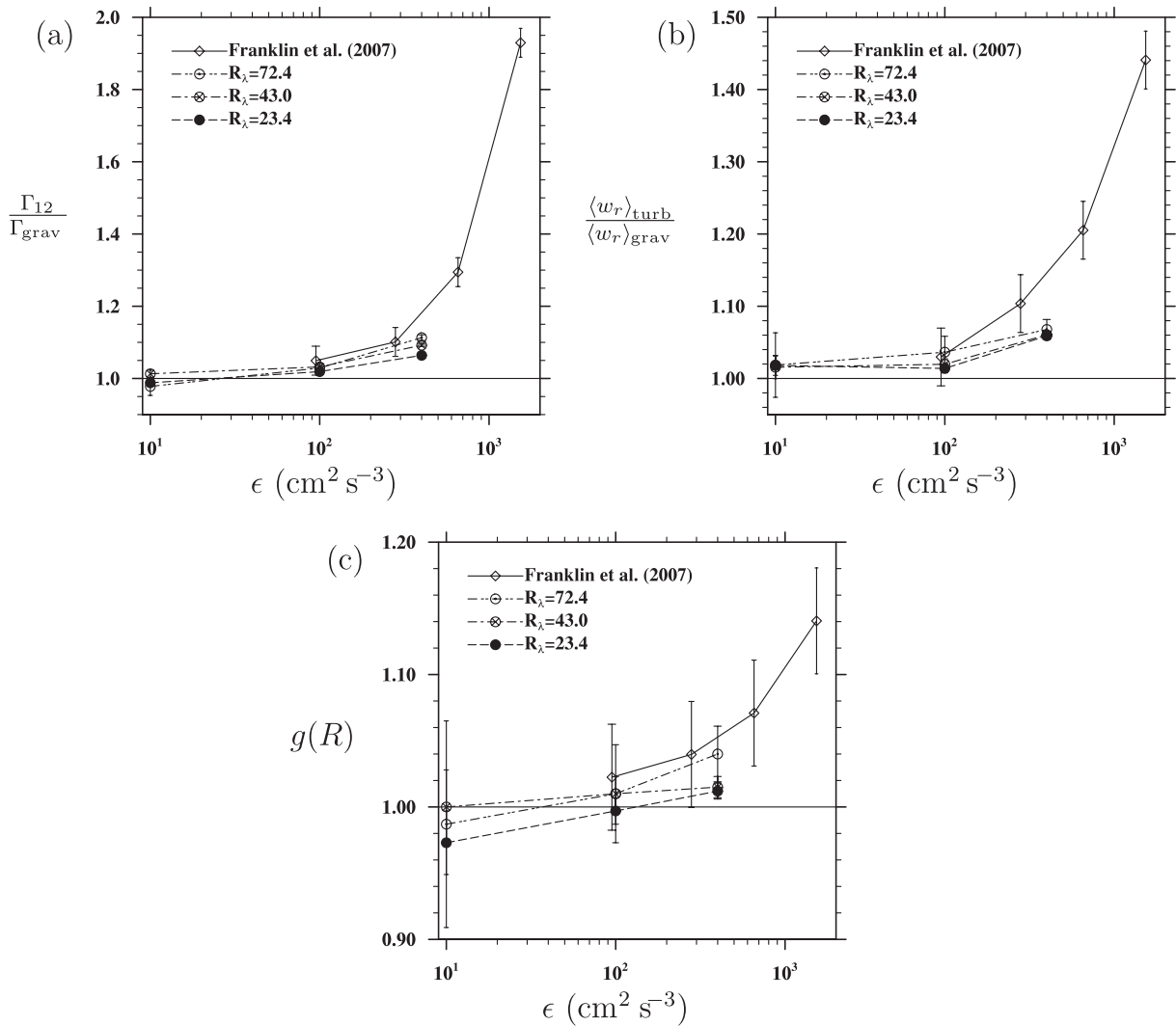


Figure 5. Comparison of our DNS results with some DNS data taken from Franklin *et al* [51]: (a) normalized collision kernel, (b) radial relative velocity and (c) RDF as a function of energy dissipation rate, for the bidisperse pair of $a_1 = 30 \mu\text{m}$ and $a_2 = 10 \mu\text{m}$.

of Franklin *et al.* Quantitatively, the Franklin *et al* results on collision rate and relative velocity appear to be somewhat larger than our results. This quantitative difference could be due to the different forcing schemes (random forcing versus deterministic forcing) used in our DNS and in the work of Franklin *et al*, as noted in the introduction. Taken together, the dependence of collision kernel and kinematic pair statistics on the flow dissipation rate is nonlinear, with increasing slope at high flow dissipation rate.

In figure 6, we compare our DNS data on dynamic collision kernel with data taken from Pinsky *et al* [61]. The latter was based on a statistical formulation of turbulence and a leading order expansion of the droplet relative motion. The two results agree with one another to within 10% and both show that the collision kernel increases with the flow dissipation rate. Note that our collision kernel includes the effect of RDF, but the data from Pinsky *et al* [61] are for the

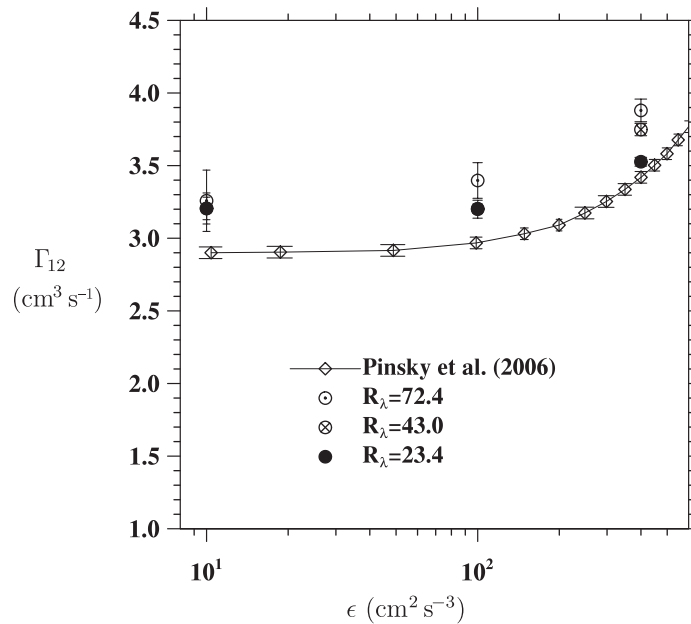


Figure 6. Comparison of our DNS results on dynamic collision kernel with data taken from figure 8(a) in Pinsky *et al* [61], for colliding pairs with $a_1 = 15 \mu\text{m}$ and $a_2 = 10 \mu\text{m}$.

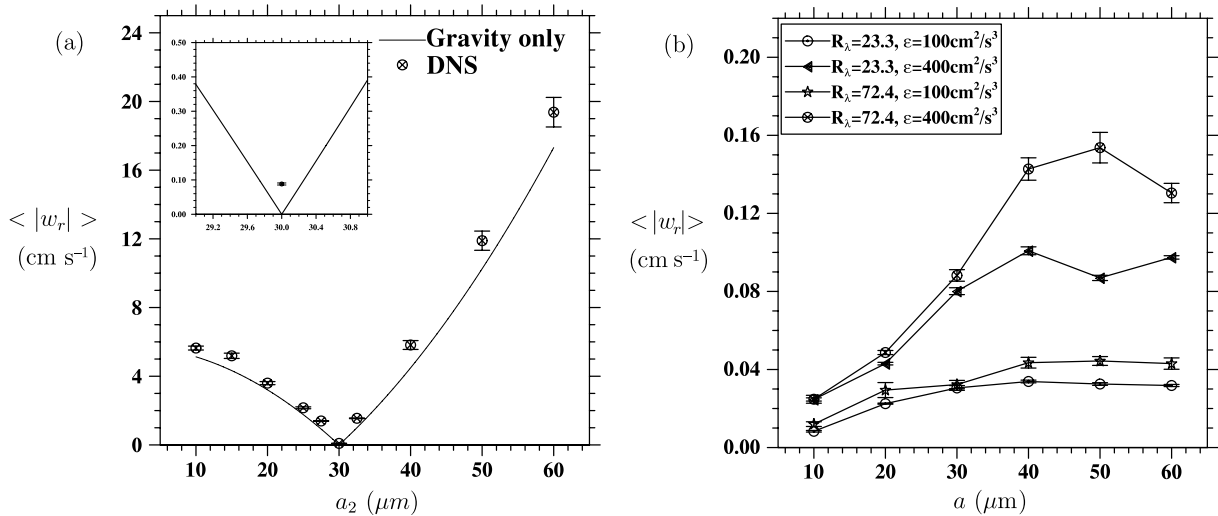


Figure 7. Radial relative velocity of droplets in turbulent flow: (a) bidisperse pairs with $a_1 = 30 \mu\text{m}$, $R_\lambda = 72.41$ and $\epsilon = 400 \text{cm}^2 \text{s}^{-3}$; (b) monodisperse pairs (i.e. $a_1 = a_2 = a$).

swept volume excluding the contribution from RDF. This may account for part of the difference between the two results.

Figure 7 shows the radial relative velocity (cm s^{-1}) as a function of droplet radius. The top figure shows results for bidisperse pairs at contact as a function of a_2 when a_1 is set to $30 \mu\text{m}$. The results are compared to the pure gravitational value. Clearly, the differential

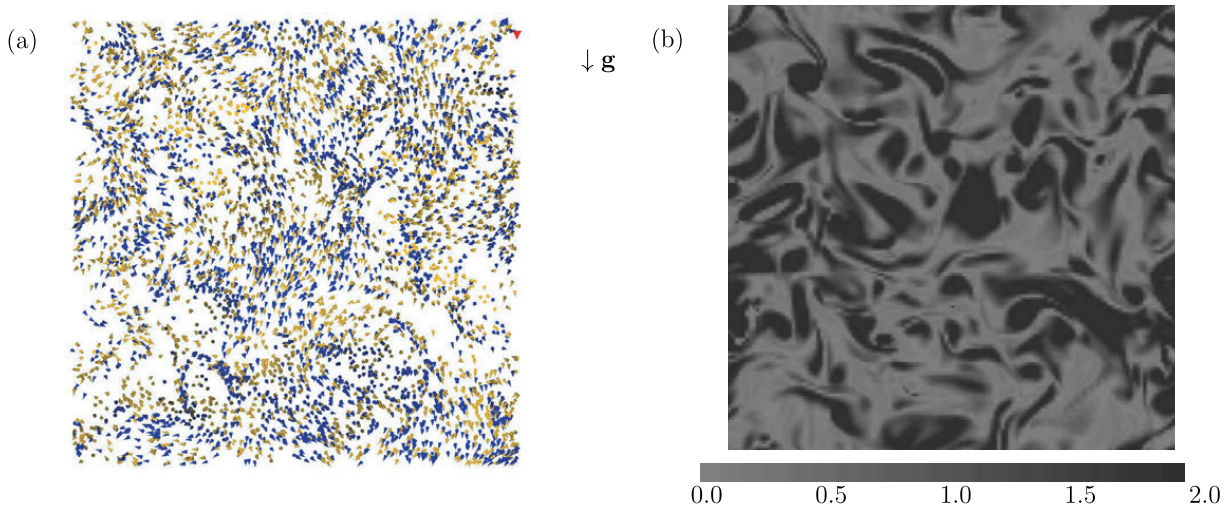


Figure 8. A snapshot from DNS of droplet position (left panel) and normalized flow entropy (right panel) on the same planar slice. Left panel: the locations of droplets of $20\ \mu\text{m}$ radius are shown by yellow cones and those of $30\ \mu\text{m}$ by blue cones. The flow parameters are: $R_\lambda = 72.41$ and $\epsilon = 400\ \text{cm}^2\ \text{s}^{-3}$. Note that the $30\ \mu\text{m}$ droplets ($St = 0.570$) show much higher levels of preferential concentration and $20\ \mu\text{m}$ droplets ($St = 0.253$) display only a weak clustering.

sedimentation dominates the relative velocity with a very moderate but measurable (10–30%) enhancement due to air turbulence. The bottom figure shows the radial relative velocity for monodisperse pairs. Interestingly, the radial relative velocity may reach a maximum when $a_1 = a_2 = 50\ \mu\text{m}$ for the high- ϵ high- R_λ flow case. This may be qualitatively explained as follows. As the droplet size increases, both the droplet inertia and terminal velocity become larger. The inertia causes droplets to deviate from flow streamlines, thus contributing to the radial relative motion. The sedimentation, on the other hand, decreases the interaction time between a droplet and a turbulent eddy, leading to reduction of radial relative motion. These two effects compete with one another. For droplets of $50\ \mu\text{m}$ or larger, the terminal velocity is larger than the turbulent fluctuation velocity (see tables 2 and 4), so the sedimentation effect dominates the droplet–turbulent eddy interaction. The figure also shows that the relative motion increases rapidly with the intensity of turbulence as measured by the flow dissipation rate. For a given droplet size, increasing dissipation rate leads to larger St and smaller S_v (see table 3); therefore, the inertial effect is made more significant relative to the sedimentation effect, yielding a larger radial relative motion between the droplets.

Next, we examine the accumulation effect, namely, how the level of droplet clustering depends on gravity and the turbulent flow parameters. Figure 8(a) is a snapshot of droplet locations within a thin planar slice from DNS of a bidisperse case in a turbulent flow at $R_\lambda = 72.41$ and $\epsilon = 400\ \text{cm}^2\ \text{s}^{-3}$. Each droplet is represented by a cone whose tip points in the direction of the instantaneous droplet velocity vector. The size of the cone does not represent the actual droplet size, it was made larger in order for them to be visible. Two different colors are used to indicate two different droplet sizes (yellow for $20\ \mu\text{m}$ droplets and blue for $30\ \mu\text{m}$ droplets). Figure 8(b) shows, for the same slice as in figure 8(a), a contour plot of the normalized entropy $((\omega_i \omega_i)^{1/2} / \langle (\omega_i \omega_i)^{1/2} \rangle)$, where ω_i is the flow vorticity. The gray scale is defined such that the darkest color denotes at least twice the corresponding field mean and the lightest color a

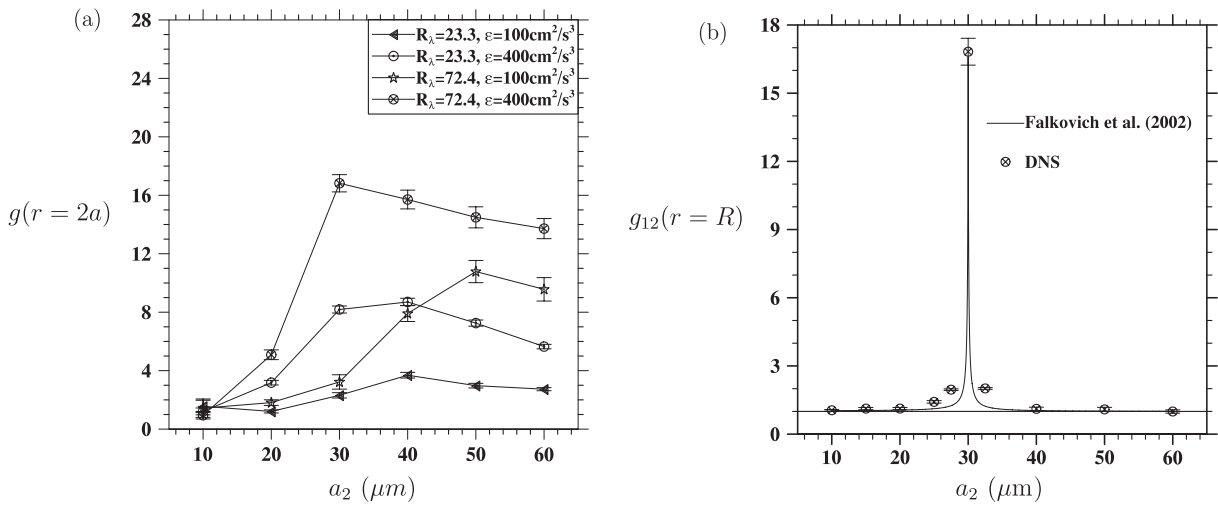


Figure 9. RDF for sedimenting droplets in turbulent flow. (a) Monodisperse case, (b) bidisperse system with $a_1 = 30 \mu\text{m}$, $R_\lambda = 72.41$, and $\epsilon = 400 \text{cm}^2 \text{s}^{-3}$.

zero local value. Figure 8(a) shows that a large percentage of droplets is moving along with the gravity direction. Some droplets are moving horizontally to avoid high-intensity vortices while falling. A few vertical patches of droplets are formed due to preferential sweeping [31]. Similar to what Zhou *et al* [49] observed for non-sedimenting droplets, we find here that sedimenting droplets of two different sizes tend to be located in somewhat different regions relative to the flow microstructures and these two sizes exhibit different levels of clustering. For sedimenting droplets, both the droplet Stokes number St and the settling ratio S_v can affect the level of clustering. Davila and Hunt [35] have proposed a new parameter to describe the combined effect of sedimentation and inertia, they showed that the interaction of sedimenting particles with vortices should be analyzed in terms of a nondimensional parameter

$$F_p \equiv \tau_p v_p^2 / \Gamma_{\text{vort}},$$

where Γ_{vort} is the circulation around a vortical region. For Stokes drag, this parameter depends very sensitively on the droplet size, namely, F_p is proportional to d_p^6 . This explains why the concentration field of $30 \mu\text{m}$ droplets can be noticeably different from that of $20 \mu\text{m}$ droplets. We believe that the level of clustering shown in figure 8(a) is more representative for sedimenting cloud droplets in strong air turbulence, than those shown in Shaw *et al* [44] for non-sedimenting particles.

Some representative results of the RDF for sedimenting droplets are shown in figure 9(a) for monodisperse pairs and in figure 9(b) for bidisperse pairs. For the case of monodisperse pairs, due to the competing effects of droplet inertia and sedimentation, the trends are similar to those for the radial relative motion shown in figure 7(b). The magnitude of monodisperse RDF depends on both the flow dissipation rate and the flow Reynolds number. For non-sedimenting particles, the maximum clustering has been found to occur for St in the order of unity [33], with maximum level to be R_λ -dependent. Here, for monodisperse sedimenting droplets, we observe a similar St -number- and R_λ -dependence. The level of monodisperse RDF is also comparable to those found in [33] for non-sedimenting particles. However, it should be noted that Wang *et al* [33] assumed $2a \approx \eta$ in their DNS, but here for cloud droplets $R \ll \eta$. Since the monodisperse RDF increases with decreasing R for $R < \eta$, the level of monodisperse RDF observed here

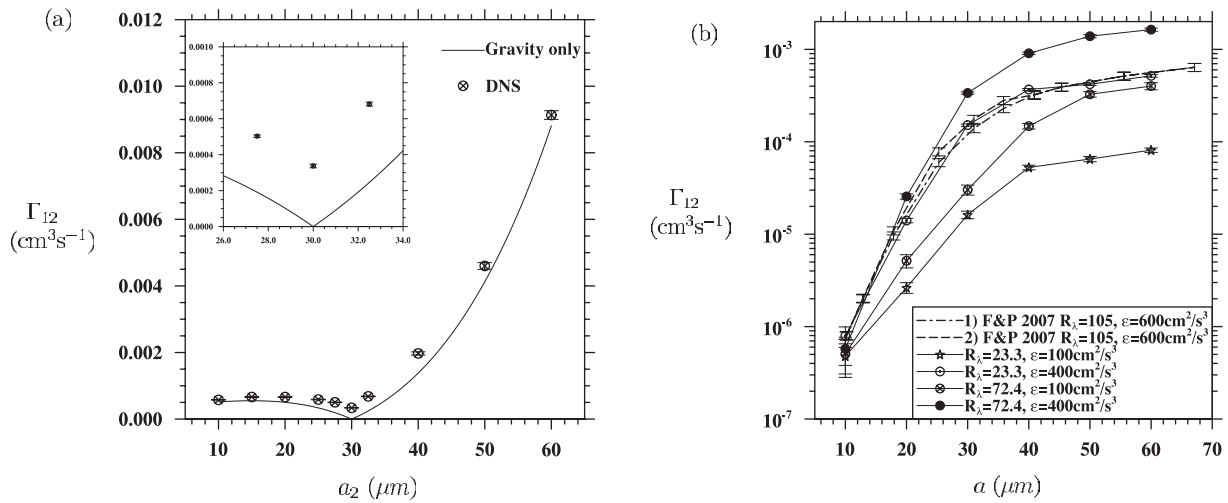


Figure 10. DNS dynamic collision kernel of sedimenting droplets in turbulent flow. (a) $a_1 = 30 \mu\text{m}$, $R_\lambda = 72.41$ and $\epsilon = 400 \text{ cm}^2 \text{ s}^{-3}$ and (b) monodisperse case.

actually implies that sedimentation tends to reduce the RDF for a given a/η . A complete quantitative study of monodisperse RDF for sedimenting droplets would be a necessary step for quantifying the collision kernel for monodisperse droplets.

More interesting results are for the bidisperse RDF $g_{12}(R)$ shown in figure 9(b). The level of $g_{12}(R)$ is much lower than the monodisperse RDF when a_1/a_2 deviates from one. This is due to the rapid decorrelation of concentration distributions for different droplet sizes. The rapid decorrelation was discussed in [33] for non-sedimenting particles. DNS of sedimenting droplets in Vaillancourt *et al* [47] showed that the level of clustering as measured by a clustering index decreases with increasing sedimentation rate. Falkovich *et al* [2] presented a theory (equation (3) in their paper) of this decorrelation for sedimenting droplets, and the results of their theory is shown in figure 9(b) for comparison. The value of the parameter α in their theory was set to 1.2 to match the monodisperse RDF. For sedimenting droplets, both the differential inertia and differential sedimentation lead to the decorrelation, so decorrelation happens much faster than the case of non-sedimenting particles. This reduction of bidisperse RDF by sedimentation can significantly reduce the importance of the accumulation effect on the collision kernel. The theory of Falkovich *et al* [2] appears to show a faster decorrelation rate than that of the DNS data.

In figure 10, we plot the geometric collision kernel as a function of droplet size. For specific flow conditions in figure 10(a), air turbulence causes a moderate (4–42%) enhancement of the collision kernel when a_2 differs from a_1 by at least $10 \mu\text{m}$. However, when a_2 is close to a_1 , the insert in figure 10(a) shows that air turbulence can double the gravitational collision kernel. For monodisperse pairs (figure 10(b)), the collision kernel increases rapidly with droplet size, flow dissipation rate and R_λ . For high- ϵ and high- R_λ , the magnitude of monodisperse collision kernel could become comparable to the bidisperse collision kernel.

Also shown in figure 10(b) are the theoretical results from Falkovich and Pumir [62] at $\epsilon = 600 \text{ cm}^2 \text{ s}^{-3}$ and $R_\lambda = 105$. The dashed line shows their prediction of the total geometric collision kernel (sum of figures 5(b) and 6 in [62]). Falkovich and Pumir [62] considered two contributions to the collision kernel: a contribution due to interaction of droplets with a local

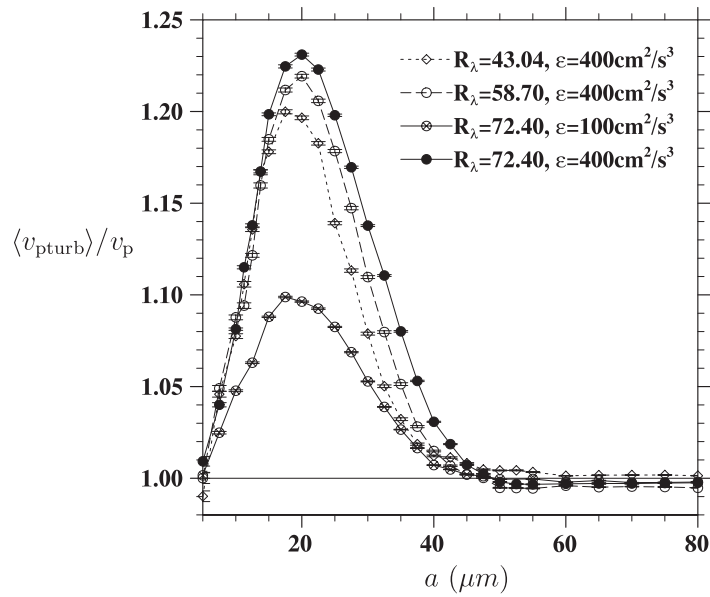


Figure 11. The average settling velocity of droplets in turbulent air, normalized by the terminal velocity in stagnant air.

flow eddy and a nonlocal contribution due to interaction of droplets with distant eddies (the sling effect). The dashed–dotted line in figure 10(b) shows the local contribution only (figure 5b from Falkovich and Pumir [62]). For the relatively low Reynolds numbers considered here, the local contribution dominates the sling component, as noted in [62]. The theory seems to predict well the overall trend, with some under-estimation of the collision kernel considering the higher dissipation rate and Reynolds number used in their analysis.

5.3. Average settling velocity

Here, we briefly discuss the increased settling velocity by turbulence. Sedimenting particles bias their trajectories toward regions of downward fluid motion around vortices and could settle significantly faster than the terminal velocity [28, 31, 35]. Figure 11 displays the ratio of average settling velocity of a droplet in turbulent flow to its terminal velocity in stagnant air. The DNS results show that large droplets ($a \geq 40 \mu\text{m}$) move in a turbulent flow at a mean velocity roughly equal to the terminal velocity.

The increased settling occurs selectively for particles with a certain range of terminal velocity and inertial response time [31, 35]. Interestingly, $20 \mu\text{m}$ droplets always exhibit the largest increase in settling velocity. This can be explained again by the theory of Davila and Hunt [35] which showed that the increased settling in vortical flow is maximized when the parameter F_p is of the order of one. For Kolmogorov eddies, $\Gamma_{\text{vort}} \approx v_k \eta = \nu$ and is independent of the flow dissipation rate. Therefore,

$$F_p = \frac{\tau_p v_p^2}{\Gamma_{\text{vort}}} = \frac{\tau_p^3 |\mathbf{g}|^2}{\nu}. \quad (13)$$

For cloud droplets in air with $\nu = 0.17 \text{ cm}^2 \text{ s}^{-1}$, we have $F_p = 0.0124, 0.794, 9.28$ and 51.6 for $a = 10, 20, 30$ and $40 \mu\text{m}$, respectively. This shows that for $20 \mu\text{m}$ droplets, the inertial response

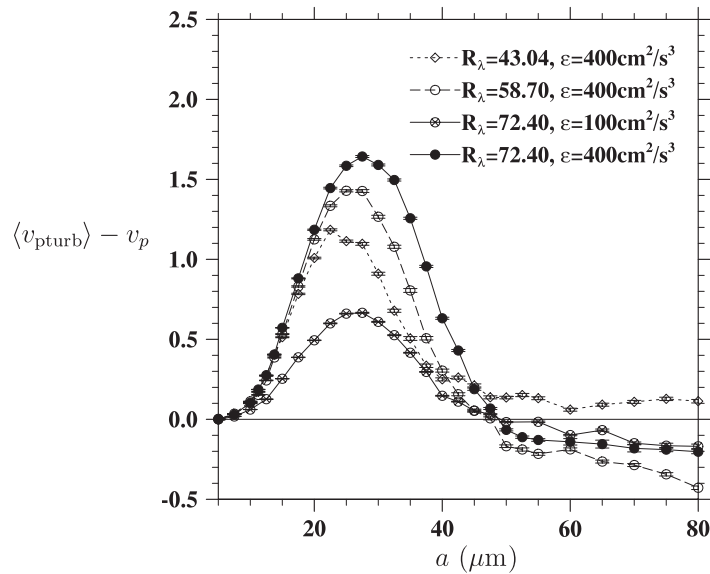


Figure 12. Difference between the average settling velocity of a droplet in turbulent flow and its terminal velocity in stagnant air.

time happens to be similar to the time (v/v_p^2) for the droplet to settle through a Kolmogorov eddy. This explains why a maximum occurs at $a = 20 \mu\text{m}$, regardless of R_λ and ϵ .

Figure 11 suggests that the collision kernel between $20 \mu\text{m}$ droplets and droplets smaller than $20 \mu\text{m}$ will be larger if this selective increase in settling is considered. In general, the increased settling is larger in magnitude $(\langle v_{\text{pturb}} \rangle - v_p)$ for $a \geq 20 \mu\text{m}$ than $a \leq 15 \mu\text{m}$ (see figure 12), so larger droplets can collect tiny cloud droplets more effectively due to the increased settling.

It has been argued that the increased settling velocities could alter the collision–coalescence growth by altering relative *mean* motion of droplets in clouds [36]. From the DNS results, we find that the relative turbulent settling velocities are larger than the relative stagnant-air settling velocities mainly for droplet-pairs with radii less than $40 \mu\text{m}$.

We mention in passing that Franklin *et al* [51] noted that in their DNS, the RDF for $20 \mu\text{m}$ collector droplet is the largest. Since the flow dissipation rates used in their work are higher, it is not possible to deduce whether their observation is related to the parameter F_p mentioned here or the higher droplet Stokes numbers at around $20 \mu\text{m}$ in their DNS. It is suggested that the parameter F_p should be considered in future studies of sedimenting droplets.

5.4. The nonlinear drag effect

In the preceding discussions, the fluid drag on the droplets has been based on a linear Stokes drag law. A better treatment may be to use a nonlinear drag of the form given by equation (3), as the droplet Reynolds number is of the order of one (see table 2). In this section, we discuss briefly the effect of such drag nonlinearity on the radial relative velocity, the RDF and the average collision kernel.

Figures 13 and 14 show the nonlinear drag effect on the results for bidisperse systems and for monodisperse systems, respectively. The difference between the results based on the

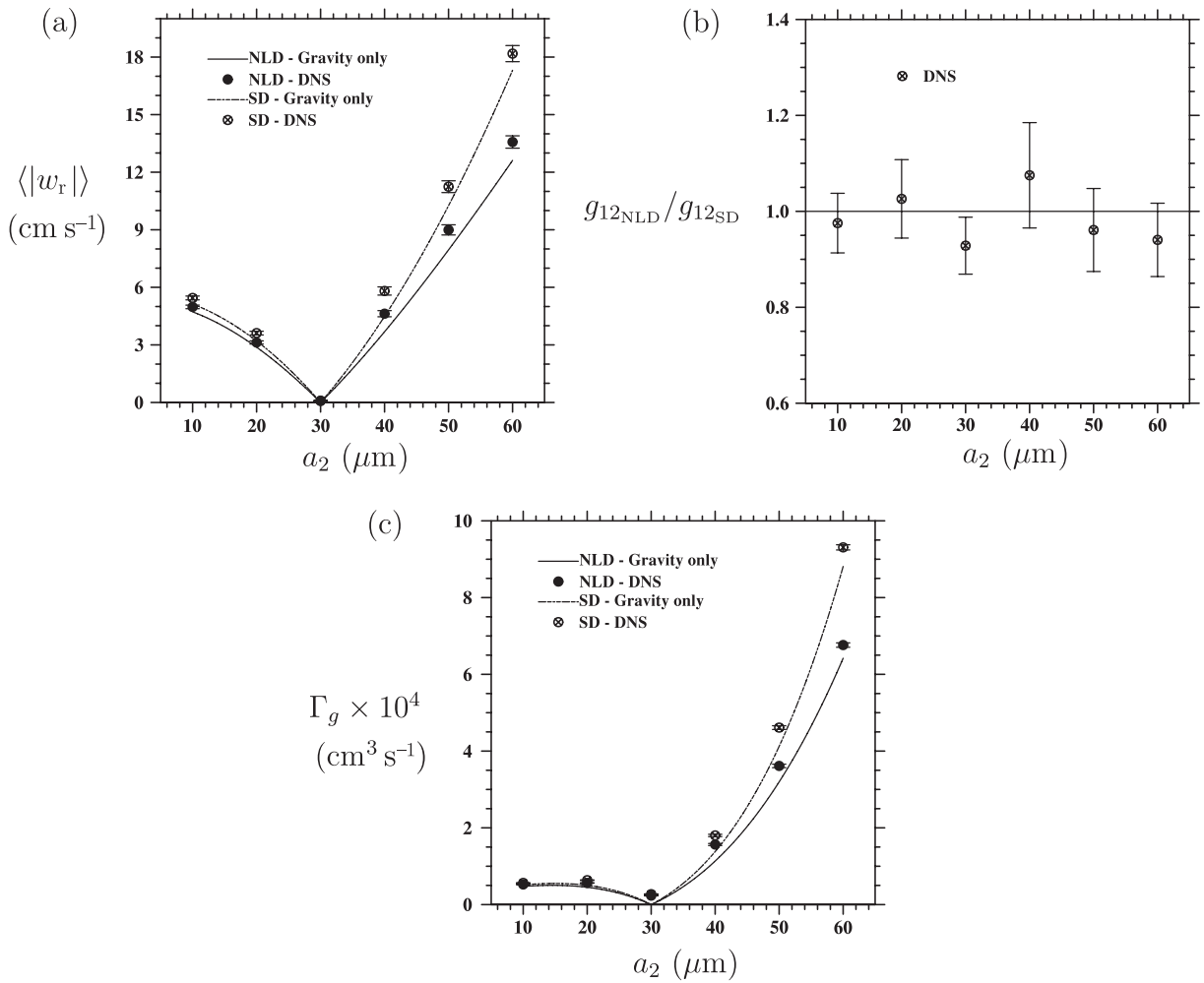


Figure 13. The effect of nonlinear drag (NLD) in bidisperse systems with $a_1 = 30 \mu\text{m}$, $R_\lambda = 43.04$ and $\epsilon = 400 \text{ cm}^2 \text{ s}^{-3}$. (a) $\langle |w_r| \rangle$, (b) $g_{12\text{NLD}}/g_{12\text{SD}}$ and (c) collision kernel.

two drag laws can be understood qualitatively by modifying the particle response time and the terminal velocity in still air as [31]

$$\tau_{\text{PNLD}} = \frac{2\rho_w a^2}{9\rho\nu f(Re_{p0})}, \quad v_{\text{PNLD}} = \tau_{\text{PNLD}} g. \quad (14)$$

Due to the nonlinear drag, the effective inertial response time τ_{PNLD} is smaller than the Stokes inertial response time τ_p , so is the effective terminal velocity. In other words, the nonlinear drag effectively reduces the size of the droplet, particularly for the larger cloud droplets where the factor $f(Re_{p0})$ is relatively larger.

For the bidisperse cases (figure 13), the droplet clustering is not significantly affected by the drag nonlinearity and the large statistical uncertainties make it difficult to draw a definite conclusion. The radial relative velocity is clearly decreased due to the reduced mean droplet terminal velocities. As a result, the collision kernel is reduced by the nonlinear drag. Similar observations were made in Franklin *et al* [51] who considered the effect of nonlinear drag for

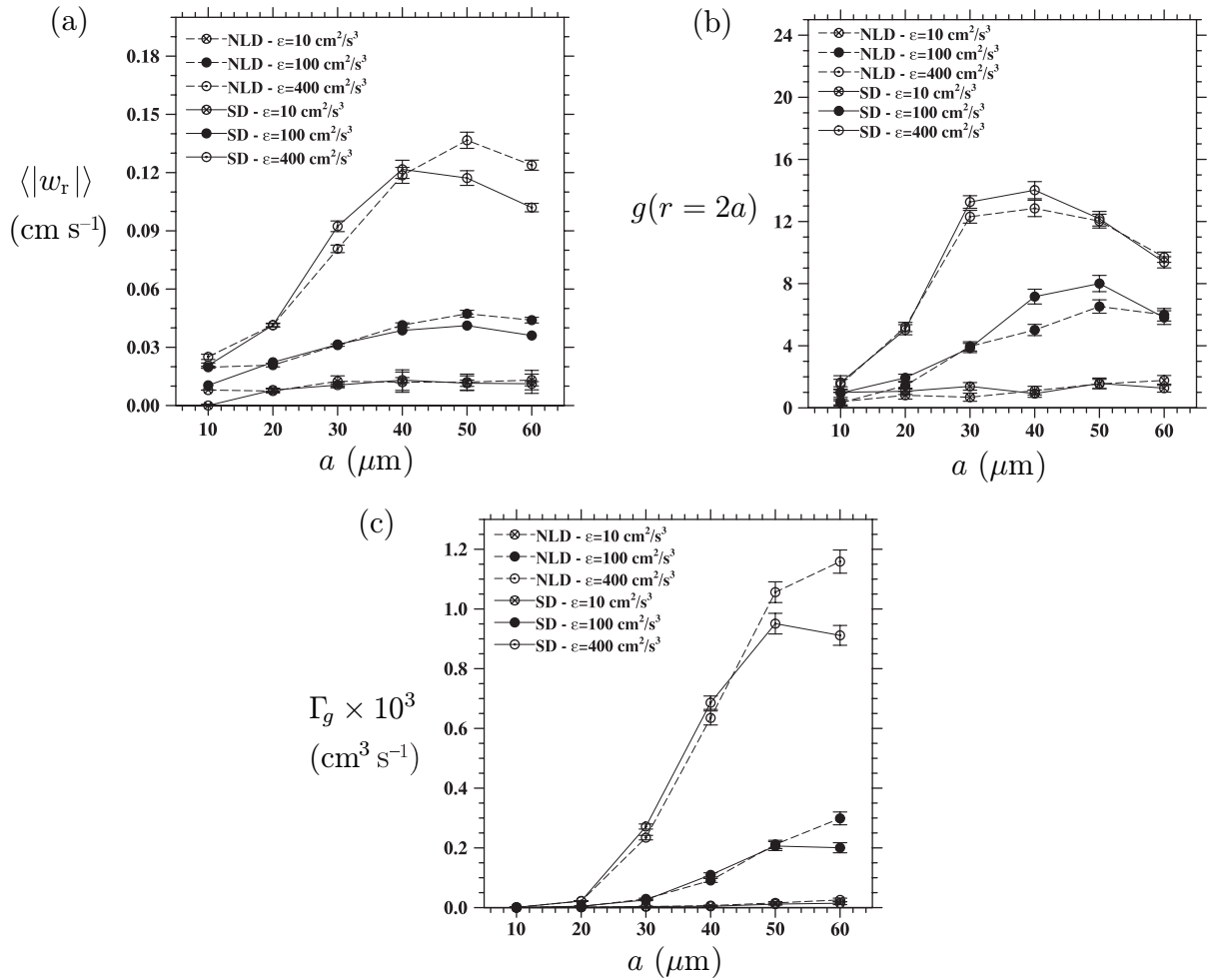


Figure 14. The effect of nonlinear drag (NLD) for monodisperse pairs. (a) $\langle |w_r| \rangle$, (b) $g(r = 2a)$ and (c) collision kernel.

collisions between 27 and 30 μm droplets at $\epsilon = 1535 \text{ cm}^2 \text{ s}^{-3}$. Our results concerning the effect of nonlinear drag are more extensive and systematic.

For monodisperse systems (figure 14), we find very little change in the radial relative velocity for droplets smaller than 30 μm as the nonlinear factor $f(Re_{p0})$ is close to unity (see table 2). For larger droplets, $\langle |w_r| \rangle$ is increased by the nonlinear drag which is contrary to the speculation by Kruis and Kusters [63] that the assumption of Stokes' law yields an overestimation of the relative particle velocity. On the other hand, Zhou *et al* [49] found an increase in the DNS collision kernel of non-settling particles due to drag nonlinearity. They argued that the nonlinear drag, which is larger than the Stokes drag, will increase the particle rms velocity rather than decrease it. This could increase the radial relative velocity. In contrast to $\langle |w_r| \rangle$, figure 14(b) shows a slight decrease in g_{12} (up to 10%). The nonlinear drag tends to increase $\langle |w_r| \rangle$ which consequently could decrease the level of particle clustering. Finally, the collision kernel is shown in figure 14(c). An interesting observation from this figure is that Γ experiences an increase for large droplets similar to the increase on $\langle |w_r| \rangle$. However, there are cases for medium-sized droplets where the collision kernel actually decreases slightly.

6. Summary and concluding remarks

We studied effects of air turbulence on the geometric collision rate of cloud droplets. The air turbulence within clouds was assumed to be homogeneous and isotropic, and its small-scale motion (from roughly 1 mm to 10 cm scales) is computationally generated by direct numerical integration of the full Navier–Stokes equations. Typical droplet and turbulence parameters of convective warm clouds are used to determine the Stokes numbers (St) and the nondimensional terminal velocities (Sv) which characterize droplet relative inertia and gravitational sedimentation, respectively. A large number of droplets forming a bidisperse system were tracked computationally, under the influence of gravity, flow drag and their own inertia. Both dynamic geometric collision events and kinematic pair statistics have been computed for 21 different droplet size combinations, three flow dissipation rates and three flow Reynolds numbers. The collection of the DNS data represents the most comprehensive study of geometric collision of sedimenting droplets. The droplet size range covered was from 10 to 60 μm .

The DNS results show that turbulence can increase the geometric collision kernel relative to the gravitational geometric kernel by as much as 47% when $\epsilon = 400 \text{ cm}^2 \text{ s}^{-3}$, due to enhanced radial relative motion (the turbulent transport effect) and preferential concentration of droplets (the accumulation effect). For smaller cloud droplets, the turbulent transport effect dominates the enhancement of collision kernel by air turbulence. For larger cloud droplets or for droplets close in size, however, the accumulation effect may become equally important. The exact level of enhancements depends on the Taylor-microscale Reynolds number, turbulent dissipation rate and droplet pair size ratio. Similar to previous observations of Franklin *et al* [49], it is found that turbulence has a relatively dominant effect on the collision process between droplets close in size as the gravitational collision mechanism diminishes. Some quantitative difference between our results and those of Franklin *et al* [51] implies that the large-scale forcing scheme may affect the collision statistics. Relative to the monodisperse system, the accumulation effect is much less important in a bidisperse system due to the rapid decorrelation of the concentration fields for different droplet sizes, in agreement with previous studies [2, 47, 49].

The noticeable dependence of the results on flow Reynolds numbers observed in this work is somewhat surprising and not fully understood. There are two possible reasons: (1) droplets respond to a range of turbulent eddies and the limited scales in DNS do not really allow separation of effects of large and small scales, (2) there exists a possibility that small-scale eddy structure is connected to large-scale eddies through non-local eddy interactions. Clearly, additional work is needed to fully resolve the effect of flow Reynolds number.

As an additional effect of turbulence on the droplet motion, we find an increase in the average settling velocity by as much as 25% when compared with the still-air terminal velocity. This increased settling centered around droplets of radius equal to 20 μm , regardless of the flow dissipation rate and Reynolds number. This confirms the analytical prediction of Davila and Hunt [35] in terms of an interaction time of a sedimenting particle with an idealized flow vortex. This selective enhancement in settling rate could have some impact on the growth of cloud droplets by collision–coalescence.

Finally, some consideration is given to the effect of nonlinear drag on the collision kernel. Drag nonlinearity was found to decrease the collision kernel by up to 26% for larger cloud droplets. For droplets less than 30 μm in radius, it was shown that the collision kernel can be accurately predicted by using the Stokes drag law.

There was evidence in this paper (e.g. figure 8) showing that the level of clustering of droplets depends sensitively on the size of droplets. For cloud droplets, both droplet inertia and terminal velocity increase with the size. It would be desirable to systematically study how the level of particle clustering and the structure of particle concentration field changes with the sedimentation parameter S_v for a given inertia parameter St or alternatively in terms of F_p , for the range of flow conditions relevant to clouds.

It should be noted that the relatively low flow Reynolds number in DNS implies that only a very limited range of scales of flow motion is explicitly represented in DNS. The relative motion and pair statistics of larger cloud droplets may be affected by larger scale fluid motion not included in our DNS. Performing DNS at higher flow Reynolds numbers in the future will eventually help resolve this uncertainty.

Acknowledgments

This study has been supported by the National Science Foundation through grants ATM-0114100 and ATM-0527140, and by the National Center for Atmospheric Research (NCAR). NCAR is sponsored by the National Science Foundation. LPW also acknowledges support from the National Natural Science Foundation of China (Project No. 10628206). We are grateful to Dr P A Vaillancourt of Meteorological Service of Canada for his helpful comments on our paper. Most of the simulations were conducted using the SGI Origin 3800/2100 and IBM clusters at NCAR. OA is grateful to the additional computing resources provided by the Scientific Computing Division at NCAR.

References

- [1] Pinsky M, Khain A and Shapiro M 1997 *J. Aerosol Sci.* **28** 1177–214
- [2] Falkovich G, Fouxon A and Stepanov M G 2002 *Nature* **419** 151–4
- [3] Riemer N and Wexler A S 2005 *J. Atmos. Sci.* **62** 1962–75
- [4] Ghosh S, Davila J, Hunt J C R, Srdic A, Fernando H J S and Jonas P 2005 *Proc. R. Soc. Lond. A* **461** 3059–88
- [5] Wang L-P, Xue Y, Ayala O and Grabowski W W 2006 *Atmos. Res.* **82** 416–32
- [6] Xue Y, Wang L-P and Grabowski W W 2008 *J. Atmos. Sci.* **65** 331–56
- [7] Pruppacher H R and Klett J D 1997 *Microphysics of Clouds and Precipitation* (Dordrecht: Kluwer Academic) p 954
- [8] Rogers R R and Yau M K 1989 *A Short Course in Cloud Physics* (New York: Pergamon) p 293
- [9] Szumowski M J, Rauber R M, Ochs H T and Miller L J 1997 *J. Atmos. Sci.* **54** 369–85
- [10] Knight C A, Vivekanandan J and Lasher-Trapp S G 2002 *J. Atmos. Sci.* **59** 1454–72
- [11] Pinsky M B and Khain A P 1997 *J. Aerosol. Sci.* **28** 1177–214
- [12] Arenberg D 1939 *Bull. Am. Meteorol. Soc.* **20** 444–5
- [13] Jonas P 1996 *Atmos. Res.* **40** 283–306
- [14] Vaillancourt P and Yau M 2000 *Bull. Am. Meteorol. Soc.* **81** 285–98
- [15] Beard K V and Ochs H T III 1993 *J. Appl. Meteorol.* **32** 608–25
- [16] Rauber R, Knight C, Ochs H and Stevens B 2003 *RICO: Rain in Cumulus over the Ocean Experiment* <http://rico.atmos.uiuc.edu/>
- [17] Lau K M and Wu H T 2003 *Geophys. Res. Lett.* **30** 2290–4
- [18] Gabilly A 1949 *Ann. Geophys.* **5** 232–4
- [19] East T W R and Marshall J S 1954 *Q. J. R. Meteorol. Soc.* **80** 26–47
- [20] Saffman P G and Turner J S 1956 *J. Fluid Mech.* **1** 16–30

- [21] Hu K and Mei R 1997 *ASME Fluid Engineering Div. Summer Meeting (June 1997)*
- [22] Wang L-P, Wexler A and Zhou Y 1998 *Phys. Fluids* **10** 2647–51
- [23] Dodin Z and Elperin T 2002 *Phys. Fluids* **14** 2921–24
- [24] Wang L-P, Ayala O and Xue Y 2005 *Phys. Fluids* **17** 067103
- [25] Manton M J 1974 *Geophys. Fluid Dyn.* **6** 83–99
- [26] Manton M J 1977 *Tellus* **29** 1–7
- [27] Reuter G W, de Villiers R and Yavin Y 1988 *J. Atmos. Sci.* **45** 765–73
- [28] Khain A P and Pinsky M B 1997 *Q. J. R. Meteorol. Soc.* **123** 1543–60
- [29] Maxey M R 1987 *J. Fluid Mech.* **174** 441–65
- [30] Squires K D and Eaton J K 1990 *Phys. Fluids A* **2** 1191–203
- [31] Wang L-P and Maxey M R 1993 *J. Fluid Mech.* **27** 27–68
- [32] Sudaram S and Collins L R 1997 *J. Fluid Mech.* **75** 337–50
- [33] Wang L-P, Wexler A and Zhou Y 2000 *J. Fluid Mech.* **415** 117–53
- [34] Wang L-P, Ayala O, Kasprzak S E and Grabowski W W 2005 *J. Atmos. Sci.* **62** 2433–50
- [35] Davila J and Hunt J C R 2001 *J. Fluid Mech.* **440** 117–45
- [36] Ghosh S and Jonas P R 2001 *Geophys. Res. Lett.* **28** 3883–6
- [37] Klett J and Davis M 1973 *J. Atmos. Sci.* **30** 107–17
- [38] Pinsky M B, Khain A P and Shapiro M 2001 *J. Atmos. Sci.* **58** 742–64
- [39] de Almeida F C 1979 *J. Atmos. Sci.* **36** 1564–76
- [40] Grover S N and Pruppacher H R 1985 *J. Atmos. Sci.* **42** 2305–18
- [41] Koziol A S and Leighton H G 1996 *J. Atmos. Sci.* **53** 1910–20
- [42] Pinsky M B, Khain A P and Shapiro M 1999 *J. Atmos. Sci.* **56** 2585–600
- [43] Pinsky M B, Khain A P and Shapiro M 2000 *Atmos. Res.* **53** 131–69
- [44] Shaw R, Reade W, Collins L and Verlinde J 1998 *J. Atmos. Sci.* **55** 1965–76
- [45] Grabowski W and Vaillancourt P 1999 *J. Atmos. Sci.* **56** 1433–6
- [46] Vaillancourt P, Yau M and Grabowski W W 2001 *J. Atmos. Sci.* **58** 1945–64
- [47] Vaillancourt P, Yau M, Bartello P and Grabowski W W 2002 *J. Atmos. Sci.* **59** 3421–35
- [48] Celani A, Falkovich G, Mazzino A and Seminara A 2005 *Europhys. Lett.* **70** 775–181
- [49] Zhou Y, Wexler A and Wang L-P 2001 *J. Fluid Mech.* **433** 77–104
- [50] Franklin C N, Vaillancourt P A, Yau M K and Bartello P 2005 *J. Atmos. Sci.* **62** 2451–66
- [51] Franklin C N, Vaillancourt P A and Yau M K 2007 *J. Atmos. Sci.* **64** 938–54
- [52] Eswaran E and Pope S B 1988 *Comput. Fluids* **16** 257–78
- [53] Sullivan N P, Mahalinggam S and Kerr R M 1994 *Phys. Fluids* **6** 1612–4
- [54] Ayala O, Rosa B, Wang L-P and Grabowski W W 2008 Effects of turbulence on the geometric collision rate of sedimenting droplets. Part 2. Theory and parameterization. *New J. Phys.* **10** 075016
- [55] Clift R, Grace J R and Weber M E 1978 *Bubble, Drops, and Particles* (New York: Academic) p 380
- [56] Ayala O, Wang L-P and Grabowski W W 2007 *J. Comput. Phys.* **225** 51–73
- [57] Allen M P and Tildesley D J 1987 *Computer Simulation of Liquids* (New York: Oxford University Press) p 408
- [58] Warshaw M 1967 *J. Atmos. Sci.* **24** 278–86
- [59] Zhou Y, Wexler A and Wang L-P 1998 *Phys. Fluids* **10** 1206–16
- [60] Wang L-P, Wexler A and Zhou Y 1998 *Phys. Fluids* **10** 266–76
- [61] Pinsky M, Khain A, Grits B and Shapiro M 2006 *J. Atmos. Sci.* **63** 2123–39
- [62] Falkovich G and Pumir A 2007 *J. Atmos. Sci.* **64** 4497–505
- [63] Kruijs F E and Kusters K A 1996 *J. Aerosol Sci.* **27** 263–4